

Neural Green’s Operators for Parametric Partial Differential Equations

H.A. Melchers

Department of Mathematics and Computer Science
Eindhoven University of Technology

h.a.melchers@tue.nl

J.H.M. Prins

Department of Applied Physics
Eindhoven University of Technology
j.h.m.prins@tue.nl

M.R.A. Abdelmalik

Department of Mechanical Engineering
Eindhoven University of Technology
m.abdel.malik@tue.nl

Abstract

This work introduces a paradigm for constructing parametric neural operators that are derived from finite-dimensional representations of Green’s operators, with learnable Green’s functions, for linear partial differential equations (PDEs). We refer to such neural operators as *Neural Green’s Operators* (NGOs). Our construction of NGOs preserves the linear action of Green’s operators on the inhomogeneity fields, while approximating the nonlinear dependence of the Green’s function on the coefficients of the PDE using neural networks that take weighted averages of such coefficients as input. This construction reduces the complexity of the problem from learning the entire solution operator and its dependence on all parameters to only learning the Green’s function and its dependence on the PDE coefficients. Moreover, taking weighted averages, rather than point samples, of input functions decouples the network size from the number of sampling points, enabling efficient resolution of multiple scales in the input fields. Furthermore, we show that our explicit representation of Green’s functions enables the embedding of desirable mathematical attributes in our NGO architectures, such as symmetry, spectral, and conservation properties. Through numerical benchmarks on canonical PDEs, we demonstrate that NGOs achieve comparable or superior accuracy to deep operator networks, variationally mimetic operator networks, and Fourier neural operators with similar parameter counts, while generalizing significantly better when tested on out-of-distribution data. For time-dependent PDEs, we show that NGOs can produce pointwise-accurate dynamics in an auto-regressive manner when trained on a single time step. Finally, we show that we can leverage the explicit representation of Green’s functions returned by NGOs to construct effective matrix preconditioners that accelerate iterative solvers for PDEs.

1 Introduction

In this paper, we consider the problem of inferring the solution operator, associated with a parametric family of partial differential equations (PDEs), from data. Generally, the task of approximating such solution operators plays a fundamental role in the development of computational methods for solving the underlying PDEs [1, 2] that appear in various areas of science and engineering. Typical examples include computational fluid dynamics [3], fluid-structure interaction [4] and solid mechanics [5]. However, finding analytical expressions of such solution operators is generally not feasible, and numerical approximations of such operators can be computationally prohibitive due to their high-dimensional and nonlinear nature [1]. Recent advances

in operator learning techniques [6] address this challenge by using data to approximate solution operators to PDEs. Typically, the data comprises instantiations of solutions to the PDE and the corresponding PDE input functions, such as boundary conditions, PDE coefficients and external forcings. The inference problem is to find the operator that maps the PDE parameters to the solution. If such a mapping is inferred, we are able to evaluate it and recover solutions of the PDE for different input parameters.

By virtue of their generalization of standard neural networks [7] to mappings between function spaces instead of between discrete vector spaces, neural operators (NOs) [6] provide a suitable representation of PDE solution maps. Representation of operators by NOs can be roughly divided into two categories. The first approach expands the output function in terms of the dot product between two vectors that are returned from two sub-networks, the so-called *branch* and *trunk* networks, which accept as arguments samples of the input functions and spatial coordinates, respectively. The second approach adds an integral operator to the discrete affine transformation in a standard neural network which allows application of the NO to varying resolutions of the input and output functions. The former construction is due to work in [8] and was extended to Deep Operator Networks (DeepONets) in [9], while the latter construction was developed for different choices of the nonlocal kernel functions such as the Fourier [10], multipole [11] and graph [12], neural operators (FNOs, MNOs and GNOs, respectively). Both such approaches received considerable research attention, and significant work has been devoted to their extensions and improvements [6]. Moreover, both approaches have been successfully applied to approximating solutions to PDEs in various fields, such as PDEs for fluid mechanics [13], fluid-structure-interaction [14], solid mechanics [15] and quantum mechanics [16]. While the errors incurred by such NOs generalize well to unseen PDE parameters within the training distribution, extrapolation beyond that distribution may become unreliable [17]. The lack of reliability in extrapolation may preclude the adoption of NOs, particularly when training data may be limited, e.g. in applications where the PDE parameters vary across length and time scales while training data may only cover a subset of those scales. Moreover, such generalization errors may be compounded when such NOs are used in an auto-regressive manner, such as predicting long-time behavior when trained on short trajectories [18, 19, 20]. Furthermore, standard application of such NOs [21, 9, 10] require point samples of the PDE parameters as input which scales unfavorably with the number of trainable parameters. This may result in inefficient models for multi-scale systems where a dense sampling of input functions is required.

In this work, we turn our attention to linear PDEs where the corresponding solution operator reduces to the Green's operator with the Green's function as the corresponding kernel [22]. We introduce a paradigm for constructing NOs that are derived from a finite-dimensional approximation of parametric Green's operators with a learnable Green's function. We refer to such NOs as *Neural Green's Operators* (NGOs). Our construction of NGOs reduces the complexity of the operator learning problem by preserving the correct linear dependence of the solution on the PDE's inhomogeneity fields (such as forcing and boundary conditions). Moreover, taking weighted averages, rather than point samples, of input functions decouples the network size (in terms of the number of trainable parameters) from the number of sampling points, enabling efficient resolution of multiple scales in the input fields. Furthermore, our construction of NGOs is conducive to including additional mathematical structure, or inductive bias [23], to preserve salient properties of the solutions to the PDE, like symmetries, spectral properties and conservation laws. We demonstrate that:

1. NGOs enable efficient approximations of PDE solutions in the sense that for roughly the same number of trainable network parameters, NGOs are on par with or more accurate than DeepONets, VarMiONs, and FNOs, and generalize significantly better to out-of-distribution problems.
2. NGOs can produce pointwise-accurate dynamics of time-dependent PDEs in an auto-regressive manner over arbitrarily large numbers of time steps, when trained on a single time step only.
3. The Green's functions inferred from NGOs can be used to construct effective matrix preconditioners for numerical PDE solvers.

The remainder of this paper is organized as follows: Section 2 introduces Green's operators for parametric PDEs and corresponding finite-dimensional representations of the Green's function. In Section 3, we introduce variants of NGO architectures for different modeling scenarios. In Section 4, we describe a canonical elliptic PDE problem and the corresponding data generation and training procedure. Section 4.3 provides results on the model accuracy, the effect of quadrature, and computational efficiency. Additionally, we

demonstrate that the learned Green's functions can be used to construct effective preconditioners. In Section 5, we test our NGO framework on some non-elliptic PDE problems. We end with a concluding discussion in Section 6.

2 Parametric Green's Operators and Functions

In this paper, we consider a linear boundary value problem in a bounded domain $\Omega \subset \mathbb{R}^d$ with a piecewise smooth boundary $\Gamma = \bigcup_i \Gamma_i$:

$$\begin{aligned}\mathcal{L}[\theta]u(\mathbf{x}) &= f(\mathbf{x}), \quad \forall \mathbf{x} \in \Omega, \\ \mathcal{B}_i[\theta]u(\mathbf{x}) &= g_i(\mathbf{x}), \quad \forall \mathbf{x} \in \Gamma_i,\end{aligned}\tag{2.1}$$

where $u(\mathbf{x})$ denotes the unknown, $\mathcal{L}[\theta]$ is a linear differential operator, parameterized by some spatially varying coefficient $\theta(\mathbf{x})$, $f(\mathbf{x})$ is a source term, $\mathcal{B}_i[\theta]$ is a boundary operator, and g_i is the data on the boundary Γ_i .

To find an expression for the unknown $u(\mathbf{x})$, we write (2.1) in weak form by testing the first equation of (2.1) against some suitable function v :

$$\int_{\Omega} v \mathcal{L}[\theta]u \, d\mathbf{x} = \int_{\Omega} v f \, d\mathbf{x}.\tag{2.2}$$

Using integration by parts and substituting the boundary conditions we may arrive at the formulation

$$B[v, u] = L[v],\tag{2.3}$$

where

$$B[v, u] = \int_{\Omega} u \mathcal{L}^*[\theta]v \, d\mathbf{x} - \sum_i \int_{\Gamma \setminus \Gamma_i} (\mathcal{B}_i[\theta]u)(\tilde{\mathcal{B}}_i v) \, d\mathbf{x},\tag{2.4}$$

and

$$L[v] = \int_{\Omega} v f \, d\mathbf{x} + \sum_i \int_{\Gamma_i} g_i \tilde{\mathcal{B}}_i v \, d\mathbf{x}.\tag{2.5}$$

Here, \mathcal{L}^* is the adjoint operator of \mathcal{L} , and $\tilde{\mathcal{B}}_i$ are boundary operators that appear in the integration by parts. For example derivations of this form, see Appendix A.

We can derive an expression for the unknown $u(\mathbf{x})$ by setting v in (2.3) to be the Green's function $G[\theta](\mathbf{x}, \mathbf{x}')$ that satisfies

$$\begin{aligned}\mathcal{L}^*[\theta]G[\theta](\mathbf{x}, \mathbf{x}') &= \delta(\mathbf{x} - \mathbf{x}'), \quad \forall \mathbf{x} \in \Omega, \\ \tilde{\mathcal{B}}_i G[\theta](\mathbf{x}, \mathbf{x}') &= 0, \quad \forall \mathbf{x} \in \Gamma \setminus \Gamma_i.\end{aligned}\tag{2.6}$$

Then, (2.3) reduces to

$$u(\mathbf{x}) = \mathcal{G}[\theta, f, g_i](\mathbf{x}) := \int_{\Omega} G[\theta]f \, d\mathbf{x}' + \sum_i \int_{\Gamma_i} g_i \tilde{\mathcal{B}}_i G[\theta] \, d\mathbf{x}',\tag{2.7}$$

and \mathcal{G} denotes the Green's operator that maps the PDE coefficient $\theta(\mathbf{x}')$, forcing $f(\mathbf{x}')$ and boundary data $g_i(\mathbf{x}')$ onto the solution $u(\mathbf{x})$ [22].

To derive a finite-dimensional approximation of the solution, we consider an expansion of the Green's function in terms of a test basis $\psi_n(\mathbf{x}')$ and trial basis $\phi_m(\mathbf{x})$:

$$G[\theta](\mathbf{x}, \mathbf{x}') \approx \phi_m(\mathbf{x}) A_{mn}[\theta] \psi_n(\mathbf{x}'),\tag{2.8}$$

where A_{mn} depends nonlinearly on θ . Substitution of (2.8) into (2.7) gives the corresponding approximation of the Green's operator

$$\mathcal{G}[\theta, f, g_i](\mathbf{x}) \approx \phi_m(\mathbf{x}) A_{mn}[\theta] d_n[f, g_i],\tag{2.9}$$

where

$$d_n[f, g_i] = \int_{\Omega} \psi_n f \, d\mathbf{x}' + \sum_i \int_{\Gamma_i} g_i \tilde{\mathcal{B}}_i \psi_n \, d\mathbf{x}'.\tag{2.10}$$

Remark 1. In a Galerkin approximation setting, the matrix A_{mn} in (2.8) represents the inverse of the system matrix.

Remark 2. While our approximation of the Green's function in (2.8) conforms to a Petrov-Galerkin method where the test functions ψ and trial functions ϕ are not the same, we may opt for a (Bubnov-)Galerkin setting for our NGO, where ϕ and ψ are the same.

3 Neural Green's Operators (NGOs)

We now define a Neural Green's Operator, based on the approximation in (2.8) with a learnable matrix, and fixed test functions $\psi(\mathbf{x}')$ and trial functions $\phi(\mathbf{x})$:

$$\hat{u}(\mathbf{x}) = \hat{\mathcal{G}}[\theta, f, g_i](\mathbf{x}) \equiv \phi_m(\mathbf{x}) \hat{A}_{mn}(\mathbf{F}[\theta]) d_n[f, g_i], \quad (3.1)$$

where 'hats' indicate quantities approximated by a neural network, and d_n is given by (2.10). The NGO is of the family of Chen&Chen [8] neural operator architectures (DeepONets, VarMiONs), in the sense that the NGO utilizes an approximation of the solution in terms of basis functions $\phi_m(\mathbf{x})$ and coefficients $\hat{u}_m \equiv \hat{A}_{mn} d_n$. We summarize the NGO architecture in Figure 1. $\mathbf{F}[\theta]$ is the input to the system net, which

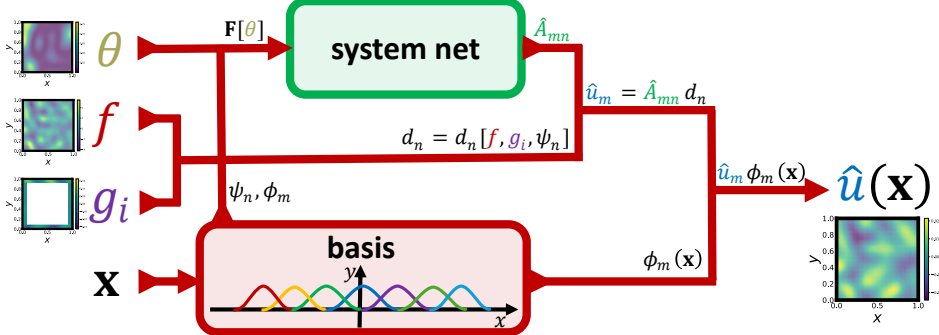


Figure 1: Architecture of the neural Green's operator (NGO), that maps the material parameter $\theta(\mathbf{x})$, forcing $f(\mathbf{x})$ and boundary conditions $g_i(\mathbf{x})$ onto the solution $u(\mathbf{x})$. For a model NGO, \mathbf{F} is given by (3.2), whereas for a data NGO, \mathbf{F} is given by (3.5). The system network, shown in blue, is the only trainable component in the NGO.

is some functional of θ . Based on the specific form of $\mathbf{F}[\theta]$, and the way the model is trained, we distinguish between three types of NGOs.

3.1 Different types of NGOs

3.1.1 Model NGO

The first type is the model NGO, where we set

$$F_{nm}[\theta] = \int_{\Omega} \phi_m \mathcal{L}^*[\theta] \psi_n d\mathbf{x}' - \int_{\Gamma \setminus \Gamma_i} (\mathcal{B}_i[\theta] \phi_m)(\tilde{\mathcal{B}}_i \psi_n) d\mathbf{x}', \quad (3.2)$$

which represents the system matrix corresponding to a discretization of (2.3). A model NGO is trained on the loss function

$$L[\hat{u}, u] = \|\hat{u} - u\|, \quad (3.3)$$

where $\|\cdot\|$ is the norm of choice in which the user wants the model to be optimal (throughout this work, we use the L^2 norm). A model NGO can be used when the target PDE (2.1) is known, and when training data is available. The theoretical lower bound of the error that an NGO may attain is given by $\|u^p - u\|$, where u^p is the projection of u onto $\phi_m(\mathbf{x})$ in the norm $\|\cdot\|$.

3.1.2 Data-free NGO

The data-free NGO can be used in the case where the target PDE is known, but solution data of the PDE is unavailable (for example, because simulations are too expensive to do). The data-free NGO exploits the similarity between an NGO and a finite element method (FEM), that would approximate $\hat{\mathbf{A}}$ as $\hat{\mathbf{A}} \approx \mathbf{F}^{-1}$. The input to the system net of a data-free NGO is still the system matrix, given by (3.2). However, the data-free NGO is trained on a loss function

$$L[\hat{\mathbf{A}}] = \|\mathbf{F}\hat{\mathbf{A}}\mathbf{F} - \mathbf{F}\|, \quad (3.4)$$

where $\|\cdot\|$ is a matrix norm of choice (we use the Frobenius norm). This loss function does not include solution data u , but instead, it steers the system net towards learning the pseudoinverse \mathbf{F}^+ of the matrix \mathbf{F} ($\mathbf{F}^+ = \mathbf{F}^{-1}$ if \mathbf{F} is invertible). The lower bound of $L[\hat{\mathbf{A}}]$ is given by $L[\hat{\mathbf{A}} = \mathbf{F}^{-1}] = 0$, which would correspond with the NGO predicting $\hat{u} = u^h$, where u^h is the solution provided by a FEM. Note that $\|u^h - u\| \geq \|u^p - u\|$ in the solution norm (3.3). In other words, a data-free NGO has a higher error bound than a model NGO.

3.1.3 Data NGO

Lastly, we consider a third type of NGO, referred to as a data NGO, which may be used if the PDE that underlies the training data is not known, but solution training data is available (for example, when dealing with experimental data). The input to the system net of a data NGO is given by

$$F_n[\theta] = \int_{\Omega} \psi_n \theta d\mathbf{x}', \quad (3.5)$$

and it is trained on the solution loss as given by (3.3). Just like for a model NGO, the data NGO error lower bound in the norm of (3.3) is given by $\|u^p - u\|$.

The use cases and characteristics of the model, data-free and data NGO are summarized in Figure 2. An

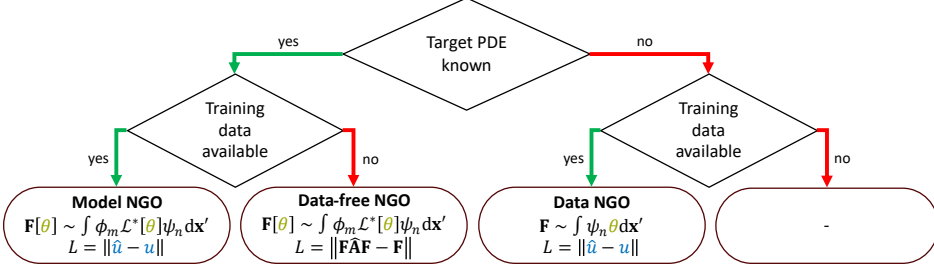


Figure 2: The use cases and characteristics of the model NGO, data-free NGO and data NGO.

important property of all three types of NGO is that they learn an approximation to the Green's function in the form of Equation (2.8), which means that the learned approximation to the Green's function can be directly extracted from a trained model. Figure 3 shows an example of the Green's function approximations as learned by an NGO. This figure shows exact Green's functions and their NGO approximations for a 1D PDE, and shows that NGOs typically learn a “smoothed” version of the Green's function, which is accurate in the low frequencies but less accurate in the high frequencies. NGOs are also not guaranteed to preserve properties of the original Green's function, such as positivity. The right-hand-side plots of Figure 3 show that the optimal approximation, given by the projection of the Green's function onto a fixed basis, has the same limitations.

Table 1 compares some key properties of the different models. NGOs are the only tested models for which (1) the input data can be given on an arbitrary set of points (provided an accurate quadrature rule is available), (2) the output can be evaluated anywhere, and (3) the linear structure of the PDE is preserved.

Remark 3. While our NGO in (3.1) uses fixed bases, we may opt to learn either the test function ψ or the trial function ϕ , or both.

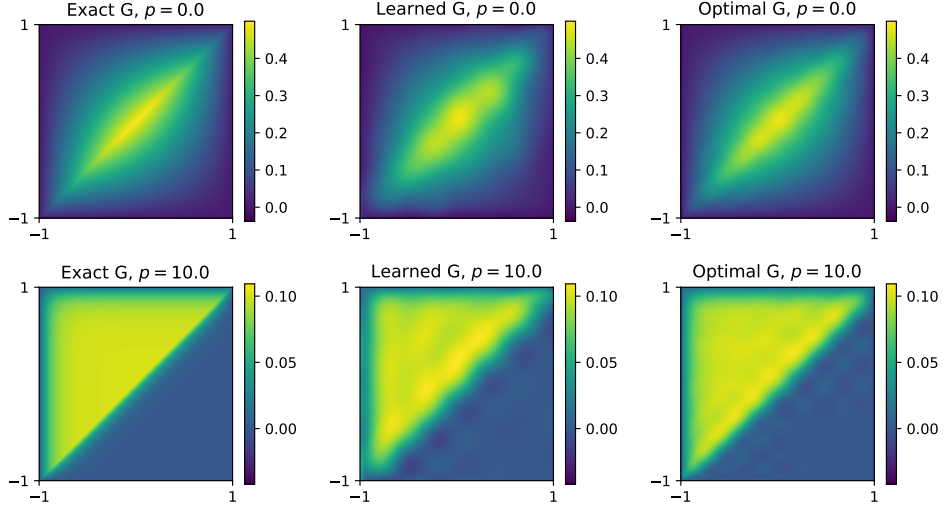


Figure 3: Left: the exact Green’s function for the 1D advection-diffusion equation $-u'' + pu' = f$, for two different values of the advection speed p . Middle: the corresponding approximations to these Green’s functions, approximated by an NGO. Right: the true Green’s functions projected onto the NGO’s basis, showing the best possible approximation of the Green’s function by an NGO.

Table 1: An overview of some key features of different neural operators.

Model	Input samples	Output samples	Linearity
DeepONet	Fixed samples	Continuous	No
VarMiON	Fixed samples	Continuous	Yes
FNO	Uniform grid	Same as input	No
UNet	Fixed uniform grid	Same as input	No
CNO	Uniform grid	Uniform grid	No
NGOs	Continuous	Continuous	Yes

Remark 4 (Relation to CNOs). A neural operator architecture similar to NGOs is the Convolutional Neural Operator (CNO). The similarities and differences between NGOs and CNOs are explained in Appendix G.

4 Test Problem: Steady diffusion

In this section, we compare the performance of the NGO with other models in literature, including DeepONets, VarMiONs, FNOs, CNOs, and U-Nets. The test equation is a steady diffusion equation on a unit square, with varying diffusion coefficient θ . The boundary conditions are Neumann boundary conditions on the top and bottom boundaries, and Dirichlet on the left and right boundaries. The equations are

$$\begin{cases} -\nabla \cdot (\theta \nabla u) = f & \text{on } \Omega = (0, L)^2, \\ \theta \nabla u \cdot \mathbf{n} = \eta & \text{on } \Gamma_N = (0, L) \times \{0, L\}, \\ \theta u = g & \text{on } \Gamma_D = \{0, L\} \times (0, L), \end{cases} \quad (4.1)$$

and a sketch of the geometry is given in Figure 4. The solution to (4.1) can be expressed in terms of the Green’s function as

$$u(\mathbf{x}) = \int_{\Omega} G[\theta](\mathbf{x}, \mathbf{x}') f(\mathbf{x}') d\mathbf{x}' + \int_{\Gamma_N} G[\theta](\mathbf{x}, \mathbf{x}') \eta(\mathbf{x}') d\mathbf{x}' - \int_{\Gamma_D} g \hat{\mathbf{n}} \cdot \nabla_{\mathbf{x}'} G[\theta](\mathbf{x}, \mathbf{x}') d\mathbf{x}'. \quad (4.2)$$

The derivation of Equation 4.2 can be found in Appendix A.1.

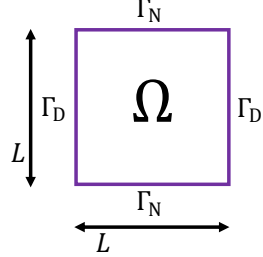


Figure 4: The square domain Ω , with Neumann boundaries Γ_N on the top and bottom, and Dirichlet boundaries Γ_D on the left and right.

4.1 NGO architecture

Using the ansatz in (2.8) to approximate the Green's function in (4.2), with $\phi_m = \psi_m$, we can approximate the solution as

$$u(\mathbf{x}) = \mathcal{G}[\theta, f, \eta, g](\mathbf{x}) \approx \phi_m(\mathbf{x}) A_{mn}[\theta] d_n[f, \eta, g], \quad (4.3)$$

where d_n is given by

$$d_n[f, \eta, g] = \int_{\Omega} \psi_n f d\mathbf{x}' + \int_{\Gamma_N} \psi_n \eta d\mathbf{x}' - \int_{\Gamma_D} g \hat{\mathbf{n}} \cdot \nabla \psi_n d\mathbf{x}'. \quad (4.4)$$

We define the NGO corresponding to (4.3) as

$$\hat{u}(\mathbf{x}) = \hat{\mathcal{G}}[\theta, f, \eta, g](\mathbf{x}) = \phi_m(\mathbf{x}) \hat{A}_{mn}(\mathbf{F}[\theta]) d_n[f, \eta, g]. \quad (4.5)$$

Here, for model NGOs and data-free NGOs, $\mathbf{F}[\theta]$ is given by the system matrix

$$F_{nm}[\theta] = - \int_{\Omega} \phi_m \nabla \cdot \theta \nabla \psi_n d\mathbf{x}' - \int_{\Gamma \setminus \Gamma_N} \theta \psi_n \hat{\mathbf{n}} \cdot \nabla \phi_m d\mathbf{x}' + \int_{\Gamma \setminus \Gamma_D} \theta \phi_m \hat{\mathbf{n}} \cdot \nabla \psi_n d\mathbf{x}', \quad (4.6)$$

which is equivalent to Equation A.4. For data NGOs, $\mathbf{F}[\theta]$ is given by

$$F_n[\theta] = \int_{\Omega} \psi_n \theta d\mathbf{x}'. \quad (4.7)$$

All neural operators were trained to learn the solution operator $(\theta, f, \eta, g) \mapsto u$.

4.2 Inductive Bias: Preconditioning the System Net

The Green's formulation of the NGO allows us to introduce additional inductive bias that may ensure preservation of certain properties of the underlying PDE, and/or enhance model accuracy. In this section, we show an example of this, where we boost the NGO's accuracy by preconditioning the output of the system net. In Section 3.1.2, we discussed the similarity between NGOs and finite element methods, and that finite element methods generally provide close to optimal approximations to the solution of a PDE. This suggests adding inductive bias to NGOs that steers the system net towards learning a matrix $\hat{\mathbf{A}}$ that is close to the inverse \mathbf{F}^{-1} of the system matrix \mathbf{F} . For model and data-free NGOs, this can be done in the following way. Suppose that the material parameters $\theta(\mathbf{x})$ are centered around and reasonably close to some average value $\langle \theta \rangle \neq 0$. Then, we can split the material parameter as

$$\theta(\mathbf{x}) = \langle \theta \rangle + \delta\theta(\mathbf{x}), \quad (4.8)$$

and, correspondingly, the system matrix as

$$\mathbf{F}[\theta] = \mathbf{F}_0 + \delta\mathbf{F}, \quad (4.9)$$

where $\mathbf{F}_0 \equiv \mathbf{F}[\langle \theta \rangle]$ and $\delta\mathbf{F} \equiv \mathbf{F}[\theta] - \mathbf{F}_0$. By factorizing out \mathbf{F}_0 as

$$\mathbf{F}[\theta] = (\mathbf{I} + \delta\mathbf{F}\mathbf{F}_0^{-1}) \mathbf{F}_0 \quad (4.10)$$

and inverting the result, we get

$$\mathbf{F}^{-1}[\theta] = \mathbf{F}_0^{-1} (\mathbf{I} + \delta \mathbf{F} \mathbf{F}_0^{-1})^{-1}. \quad (4.11)$$

Equation (4.11) can be expressed in terms of a Neumann series as

$$\mathbf{F}^{-1}[\theta] = \mathbf{F}_0^{-1} \sum_{k=0}^{\infty} (-\delta \mathbf{F} \mathbf{F}_0^{-1})^k = \mathbf{F}_0^{-1} \left[\mathbf{I} + (-\delta \mathbf{F} \mathbf{F}_0^{-1}) + (-\delta \mathbf{F} \mathbf{F}_0^{-1})^2 + (-\delta \mathbf{F} \mathbf{F}_0^{-1})^3 + \dots \right], \quad (4.12)$$

which converges if

$$\rho(-\delta \mathbf{F} \mathbf{F}_0^{-1}) < 1, \quad (4.13)$$

where ρ is the spectral radius. Equation (4.12) can be used as ansatz for $\hat{\mathbf{A}}$ as

$$\hat{\mathbf{A}}(\mathbf{F}[\theta]) \approx \mathbf{F}_0^{-1} \left[\sum_{k=0}^K (-\delta \mathbf{F} \mathbf{F}_0^{-1})^k + \text{NN}(-\delta \mathbf{F} \mathbf{F}_0^{-1}) \right], \quad (4.14)$$

where NN is the system net. \mathbf{F}_0^{-1} effectively acts as a preconditioner, and the system net within the Neumann series ansatz effectively learns a correction to a truncated Neumann series of order K . To minimize computational overhead, we choose $K = 1$. Then, using the Neumann series ansatz in an NGO comes at the cost of computing a *single, offline* matrix inverse \mathbf{F}_0^{-1} and two online matrix-matrix products only. Figure 5(a) shows that a Neumann model NGO effectively learns about two additional terms to a Neumann series truncated at order K , compared to a FEM that uses the same truncated Neumann series for approximate matrix inversion. Figure 5(b) shows that the Neumann NGO error indeed scales with the spectral radius ρ of $-\delta \mathbf{F} \mathbf{F}_0^{-1}$. However this turns out to be the case for both Neumann model NGOs, and vanilla model NGOs.

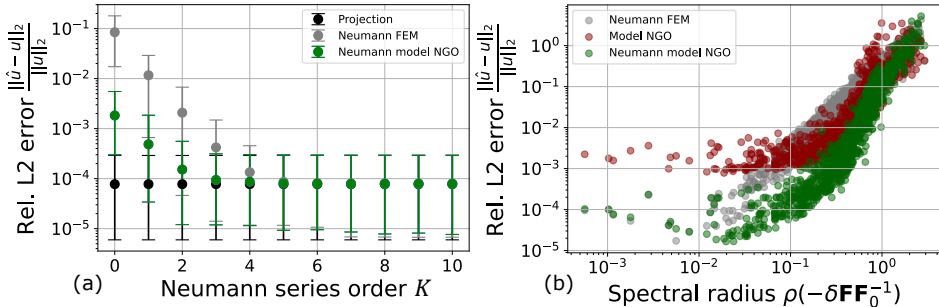


Figure 5: (a) Relative L^2 test error versus the order K of the truncated Neumann series of a FEM that uses an approximate matrix inversion using a Neumann series, and a Neumann model NGO as defined in (4.14). (b) The relative L^2 test error versus the spectral radius $\rho(-\delta \mathbf{F} \mathbf{F}_0^{-1})$ for a vanilla model NGO, and a Neumann model NGO. the models have been trained on dataset C (Appendix B). Points and error bars are, respectively, averages and 95% confidence intervals on 1000 manufactured steady diffusion solutions, generated in the same way as dataset C.

Another example of inductive bias that we embed in the NGO formulation is the scale equivariance of the steady diffusion equation 4.1 with respect to its material parameter θ , which we can express as

$$\mathcal{L}[c\theta] = c\mathcal{L}[\theta], \quad \forall c \in \mathbb{R}^+, \quad (4.15)$$

where c is a positive constant. In Appendix E, we show how to embed this symmetry into the NGO formulation, and we demonstrate its effect on the NGO's generalization error across different material parameter scales.

4.3 Results

In the next section, we compare the performance of the NGO in (4.5) to that of a number of other models: VarMiONs, DeepONets, FNOs, CNOs, and U-Nets.

4.3.1 Generalization Errors of Different NOs

Table 2 shows the error percentages achieved by the trained models on in-distribution and out-of-distribution testing data. Dataset A is used for training data and in-distribution testing data, while dataset B is used for out-of-distribution data (see B.1 for a description of the different data sets). The exact architectures of these models are given in Appendix C.1.1. The details of the training procedure are given in Appendix D.1. Figures 6a and 6b show samples from both data sets.

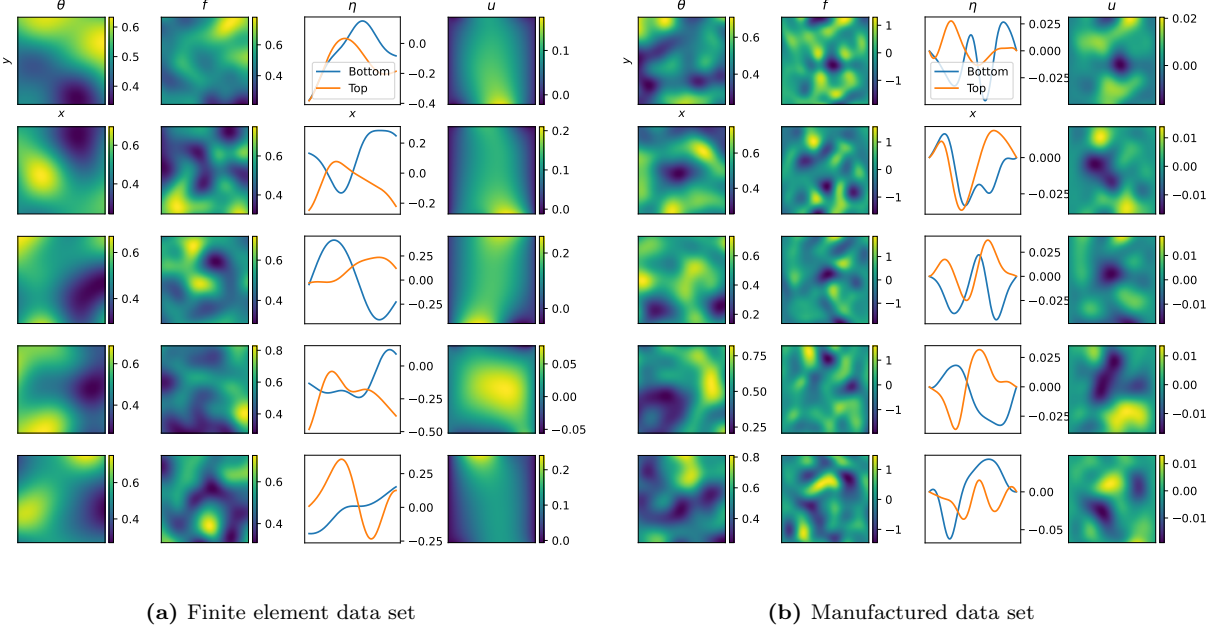


Figure 6: Five random samples of solutions from the finite element data set (top) and the manufactured data set (bottom).

The errors are given in terms of mean and standard deviation of the relative L^2 error. We define the relative L^2 error as $e_i = \frac{\|\hat{u}^{(i)} - u^{(i)}\|_{L^2(\Omega)}}{\|u^{(i)}\|_{L^2(\Omega)}}$, where $u^{(i)}, i = 1, \dots, N$ are the true solutions and $\hat{u}^{(i)}$ are the model predictions.

As a reference, Table 2 also includes the accuracy obtained by the Galerkin Finite Element Method (FEM) using the same 12×12 cubic B-spline basis functions, as well as the error obtained by projecting the true solutions onto the span of the basis functions. The ‘‘Projection’’ entry is the lowest possible error achievable by any model using these basis functions. The final entry, ‘‘POD-Galerkin’’, refers to the Galerkin method using the first 144 POD modes of the training data as a function basis.

Figure 7 shows the predictions made by the four NGO models and the five reference models, when tested on in-distribution data (Figure 7a) and out-of-distribution data (Figure 7b). Note that all models perform well on the in-distribution data, producing approximate solutions that are visually indistinguishable from the true solution. However, with exception of the VarMiON, the reference models fail to generalize to out-of-distribution data, instead producing predictions with greater than 100% relative error. A noteworthy observation is that the U-Net, the only tested model that does not use a basis but instead acts on pointwise values only, fails to produce smooth functions as output.

4.3.2 Generalization Errors Across Length Scales

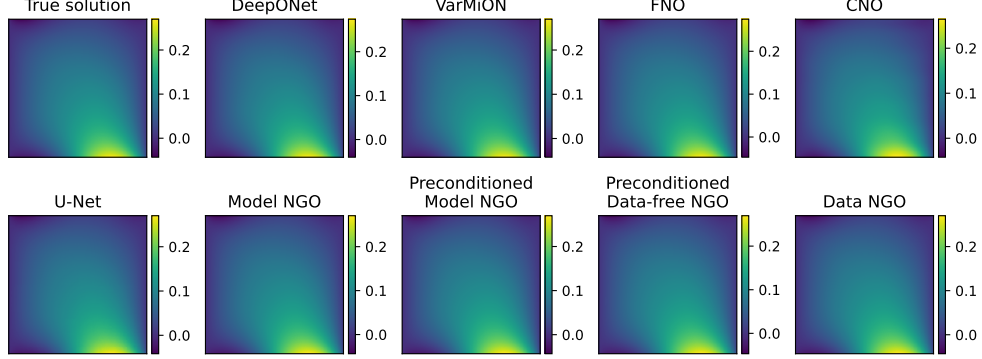
In this section, we compare the NGOs against other models from literature in their ability to generalize across test data length scales. To elucidate the efficacy of the NGO construction that mimics the action of the Green’s operator, depicted in Figure 1, we compare the performance of NGOs against DeepONets

Table 2: Accuracy of the tested models on different data sets. The ‘Galerkin’ entry shows the solution errors of solving the PDEs with Galerkin finite elements on the B-spline basis used by the DeepONet, VarMiON, and NGOs. The ‘Projection’ entry shows the error when projecting the true solution onto the B-spline basis, which is therefore the lowest error achievable by any model using this basis.

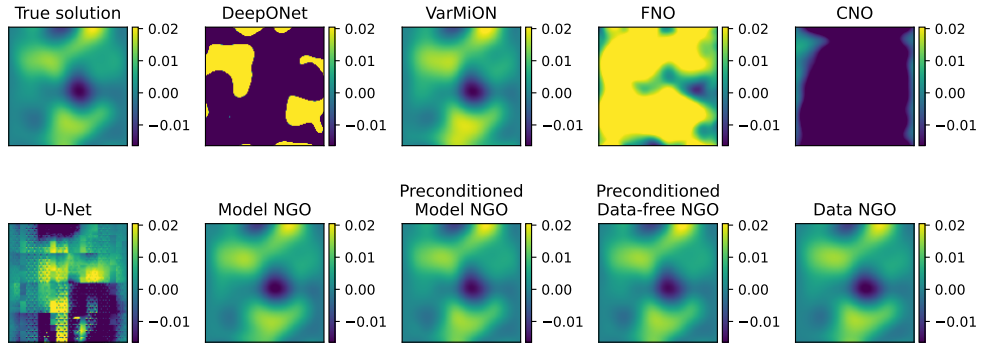
Model	Parameters	Test error	
		In distribution	Out of distribution
DeepONet	31224	0.86% \pm 0.73%	80380.83% \pm 26549.77%
VarMiON	31283	0.27% \pm 0.20%	20.53% \pm 19.37%
FNO	28975	0.31% \pm 0.16%	373.59% \pm 149.42%
CNO	28109	1.41% \pm 0.74%	774.59% \pm 193.58%
U-Net	30221	0.82% \pm 0.38%	340.80% \pm 253.54%
Model NGO	28387	0.24% \pm 0.24%	12.94% \pm 3.51%
Preconditioned model NGO	28387	0.21% \pm 0.17%	6.68% \pm 23.17%
Preconditioned data-free NGO	28387	2.82% \pm 2.83%	6.73% \pm 3.86%
Data NGO	27981	0.26% \pm 0.37%	12.07% \pm 3.73%
Galerkin		0.10% \pm 0.06%	2.76% \pm 0.74%
Projection		0.08% \pm 0.05%	2.63% \pm 0.70%
POD-Galerkin		0.03% \pm 0.02%	4.38% \pm 1.46%

and VarMiONs that use the same basis, NN architecture (for the learnable model component), number of trainable parameters and quadrature density. More specifically, we compare a DeepONet, VarMiON, data NGO, data-free NGO and model NGO that all use the same 10×10 cubic B-spline basis, all use a U-Net with approximately $3 \cdot 10^4$ trainable model parameters, and all use a quadrature grid of approximately 100×100 points. For completeness, we also report the performance of a standalone NN (U-Net) and an FNO with 10×10 Fourier modes, with approximately the same numbers of trainable parameters and quadrature points. Details of the model architectures are highlighted in Appendix C.1.2. The models have been trained on dataset C, described in Appendix B.1, using the training procedure described in Appendix D.1.2.

The results are presented in Figure 8, where the accuracies of the different NOs are compared on test datasets with varying GRF length scales λ . The models are tested on in-distribution length scales $0.5 < \lambda/L < 1$ (dataset C), as well as on out-of-distribution test data with finer length scales $0.05 < \lambda/L < 0.5$ (generated in the same way as dataset C). The black data in Figure 8 are the L^2 -projection errors, which result from projecting the true solutions onto the B-spline basis. The L^2 -projection errors are a lower bound for the errors in the solutions of the NOs that use this B-spline basis (DeepONet, VarMiON, data NGO, data-free NGO and model NGO). We observe that while smooth solutions can be accurately represented on the B-spline basis, solutions with smaller length scales are underresolved, which is also visible in the example solution and its projection, shown in the left of Figure 8. The performance of the U-Net, a baseline neural network (NN) shown in red, is evaluated when used independently. This model achieves reasonable accuracy within the training data distribution; however, its error increases significantly outside this distribution. A similar trend is observed for the FNO and the DeepONet, with the FNO exhibiting a lower in-distribution error compared to the U-Net and DeepONet. VarMiONs, by contrast, preserve the linear dependence of the solution on f , η , and g , as well as the nonlinear dependence on θ , as expressed in (4.2). The preservation of such structure explains their consistently higher accuracy compared with DeepONets and U-Nets. In contrast to VarMiONs, NGOs explicitly compute the right-hand side vector d_n rather than learning it, significantly reducing the number of trainable parameters. For VarMiONs, the learnable matrices \hat{F}_{nq} , \hat{H}_{nq} , and \hat{G}_{nq} scale with the quadrature density Q , leading to a parameter count of $\mathcal{O}(Q)$. With a fixed parameter budget of 3×10^4 , VarMiONs are restricted to an input quadrature of $Q = 10 \times 10$, which may be insufficient to capture fine-scale features in the data. NGOs, however, take weighted averages of the material parameters θ against the basis functions as input. Consequently, their parameter count depends solely on the number of basis functions N and is independent of the quadrature density Q . This independence enables NGOs to utilize arbitrarily fine quadrature at the input stage, leading to superior out-of-distribution accuracy on



(a) The true solution of one problem from the in-distribution data set, and model predictions of the different neural operators.



(b) The true solution of one problem from the out-of-distribution data set, and model predictions of the different neural operators.

Figure 7: The true solution and model predictions to one problem from the in-distribution dataset (Figure 7a) and one problem from the out-of-distribution dataset (Figure 7b).

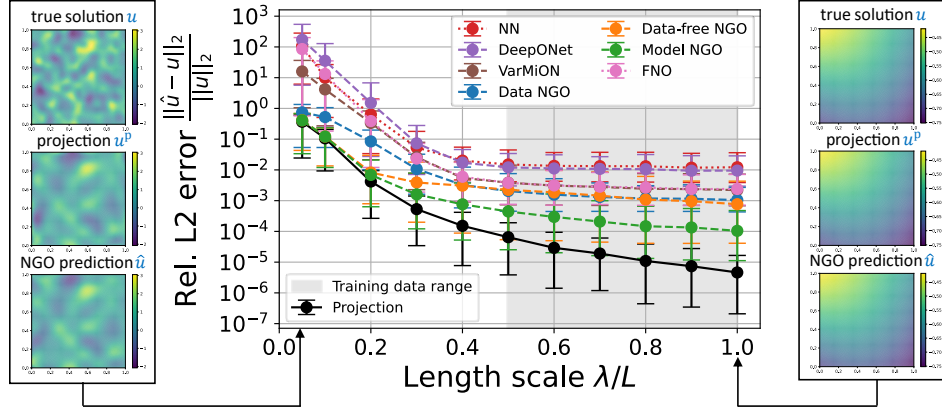


Figure 8: Relative L^2 test error versus test data length scale λ/L for a bare NN (here a U-Net), and the same NN, when used in a DeepONet, VarMiON, data NGO, data-free NGO and model NGO. All models have roughly $3 \cdot 10^4$ trainable parameters, and all models (except the NN and FNO, also added as reference) use the same 10×10 cubic B-spline basis, and are thus limited by the same L^2 projection error lower bound, indicated in black. Points and error bars are, respectively, averages and 95% confidence intervals on datasets of 1000 manufactured steady diffusion solutions, generated in the same way as dataset C.

fine-scale data. The relationship between quadrature density and model input for DeepONets, VarMiONs, and NGOs is summarized in Figure 9.

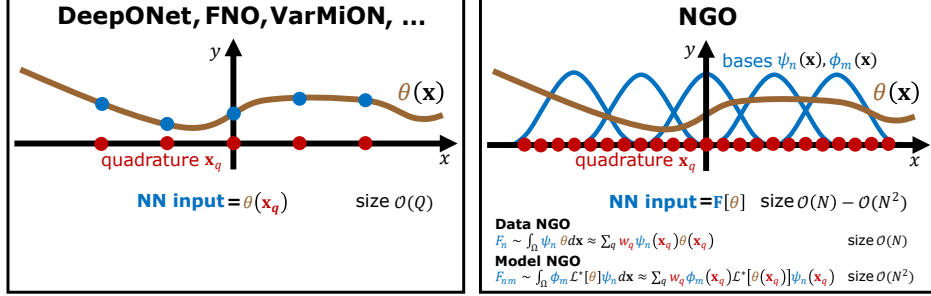


Figure 9: The input structure of an NGO compared to input structure of neural operators from literature like the DeepONet, FNO and VarMiON. Typically, the learnable components of canonical neural operators take as input the input function θ sampled on a quadrature grid \mathbf{x}_q , so the size of the input vector is determined by the number of quadrature points Q . On the other hand, the NGO system net takes as input inner products of the input function with a basis, which are computed using a quadrature rule with weights w_q and points \mathbf{x}_q . The size of the NGO input is thereby determined by the size of the basis N , and independent of the number of used quadrature points Q . Therefore, for the same NN input size (in the example illustration, 5 numbers), an NGO can use (arbitrarily) finer quadrature, resulting in higher accuracy on problems that involve fine scale data, where dense quadrature is required.

4.3.3 Comparison of Different Bases and System Network Architectures

In this section, we compare the approximation properties of NGOs that use different combinations of system net architectures and bases. Details of the model architectures are highlighted in Appendix C.1.2, and the system net architectural details can be found in Appendix C.1.3. The models have been trained on dataset C, described in Appendix B.1, using the training procedure described in Appendix D.1.2. Figures 10(a) and (b) show the effect of using different system nets and bases to approximate solutions of (4.1) on in-distribution test datasets against the errors incurred by standalone architectures and L^2 —projection errors onto the bases, respectively. The results in Figure 10(a) convey that the use of NNs as system networks within an NGO

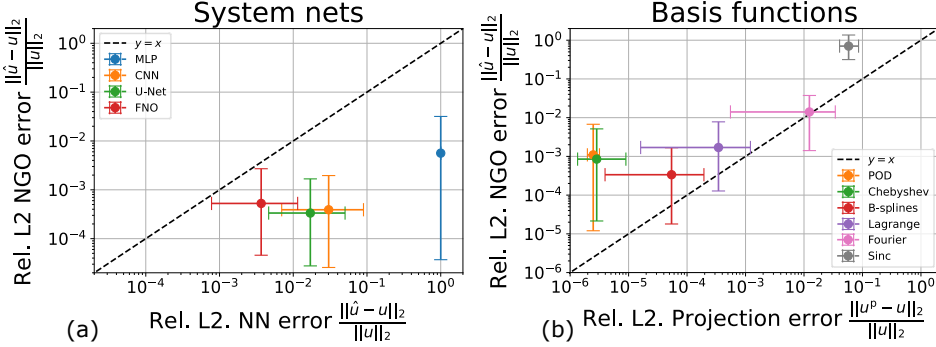


Figure 10: (a) Comparison of the error of a few canonical NN architectures when used as standalone solution approximators, versus the same NN when used as system net in a preconditioned model NGO with 10×10 cubic B-spline bases. (b) Comparison of the L^2 projection errors of solutions projected on a few canonical bases having 100 degrees of freedom, versus the error of a preconditioned model NGO with U-Net as a system network that uses the same bases. Points and error bars are, respectively, averages and 95% confidence intervals on 1000 manufactured steady diffusion solutions, generated in the same way as dataset C.

consistently outperforms their standalone use as solution approximators. For example, the errors incurred by an MLP are reduced by more than two orders of magnitude when used within a preconditioned model NGO. While the FNO is the most accurate of the standalone network architectures, the U-Net performs the best when used as system network in our model NGO. The results in Figure 10(b) convey that while more

efficient approximation spaces generally result in more accurate NGOs, we observe that the gap with respect to the L^2 -projection errors widens for POD and Chebyshev bases. This widened gap may be due to the limited expressivity of the system network or the limitations of our training process.

4.3.4 Sensitivity Analysis

In this section, we numerically analyze the sensitivity of the NGO accuracy on important model and training parameters, namely, quadrature density, size of the basis, number of trainable parameters, size of the training dataset and the number of training epochs. Details of the model architectures are highlighted in Appendix C.1.2. The models have been trained on dataset C, described in Appendix B.1, using the training procedure described in Appendix D.1.2. Figure 11 shows the resulting error curves of a data NGO, data-free NGO, model NGO, in comparison to FEM and L^2 projection. The main observation is that for all tests, the model NGO error stagnates at approximately 10^{-4} , so none of the parameters on the horizontal axes dominate the error. The discrepancy between this error and the projection error can be associated with the limited approximation capability of the used system net (here, a U-Net), or limitations of our training process. The design of a better system net and/or optimization strategy is left for future research. Another interesting observation from Figure 11(a) is that, as discussed in Section 3.1, the data-free NGO is bounded from below by the FEM error, which is not necessarily the case for data and model NGOs, and that data and model NGOs are less sensitive to assembly quadrature errors than FEM, and even projection. Final interesting observations are that for Neumann-preconditioned model NGOs, as few as $10^4 - 10^5$ trainable parameters, 10^4 training samples, and $5 \cdot 10^3$ training epochs are usually sufficient. A data NGO needs about $2 \cdot 10^4$ epochs to converge.

4.3.5 Training Speed

In addition to the accuracy of different models, we also compare the model architectures by their computational efficiency. To do this, the VarMiON, FNO, and NGO variants are benchmarked on a server with a 28-core 2.6GHz Intel Xeon Gold 6132 CPU and four NVIDIA Tesla V100 GPUs. The training performance is measured by evaluating the model on a batch of 100 samples, and also performing the backpropagation necessary for gradient-based optimization. Note that NGOs first compute inner products of the PDE parameters with the basis functions or their derivatives. This step comes at a measurable computational cost, but does not depend on any trainable parameters of the models. As such, it is possible to precompute these vectors and matrices for a given data set, and train the NGO by passing precomputed arrays to it during training. The NGO performance is tested with this optimization implemented.

Table 3 shows the training and inference performance of FNOs, VarMiONs, as well as model NGOs and data NGOs. From this, it is clear that the DeepONet is the fastest model to train, followed by the VarMiON, the U-Net, and then the NGOs. The memory usage of the NGOs is higher than that of the DeepONet and VarMiON, but lower than that of the FNOs and comparable to the CNO.

Table 3: Performance comparison, in terms of time and memory usage, of NGOs compared to FNOs and VarMiONs. For the NGOs, the benchmark takes advantage of the ability to pre-assemble the system network inputs.

Model	Computing time per batch [ms]	Peak memory usage [MB]
Model NGO	9.2	498
Data free NGO	10.7	565
Data NGO	5.5	345
DeepONet	1.1	32
VarMiON	3.7	81
FNO	106.7	4140
CNO	40.6	491
U-Net	5.2	201

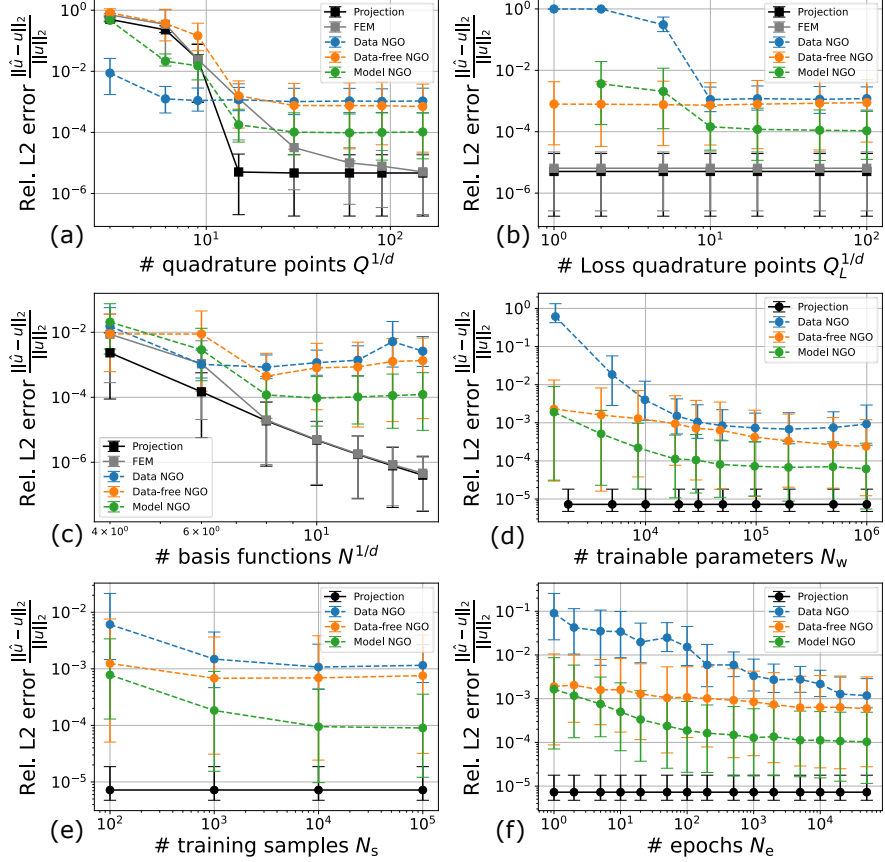


Figure 11: The relative L^2 test error of a data NGO, Neumann-preconditioned data-free NGO, and a Neumann-preconditioned model NGO, in comparison to FEM and projection errors, versus the (a) number of assembly quadrature points per dimension $Q^{1/d}$, (b) number of loss quadrature points per dimension $Q_L^{1/d}$, (c) number of basis functions N , (d) number of trainable parameters N_w , (e) number of training samples N_s , and (f) number of training epochs N_e . Points and error bars are, respectively, averages and 95% confidence intervals on 1000 manufactured steady diffusion solutions, generated in the same way as dataset C.

4.3.6 NGO-based Preconditioners

Recently, neural operators have gained interest as methods to speed up the numerical solution of PDEs, using discretizations such as finite differences or finite elements. There are multiple ways to achieve this acceleration. One method, used by Zhang et al. [24], Hu et al. [25], and Ackmann et al. [26] among others, constructs a fixed-point iteration scheme for linear systems (derived from PDEs), that alternates between a ‘‘standard’’ smoothing step, such as Jacobi or Gauss-Seidel, and an application of the respective neural operator. Others, including Kopaničáková et al. [27] and Xiang et al. [28], use the learned operator as a preconditioner directly, in combination with a linear solver such as Flexible GMRES [29] to allow non-linear operators as preconditioners for linear systems. However, neither approach is generally applicable to PDEs as they require specific choices for the solver or iteration scheme used.

An advantage of NGOs is that the fact that they learn an approximation to the Green’s function facilitates the construction of preconditioners for numerical discretizations of the same PDE. In this section, we give an example of using a trained NGO to construct a preconditioner for a finite difference discretization for the diffusion equation. Specifically, a given discretization of a PDE yields a linear system with a matrix $\mathbf{C}[\theta]$, for which we can construct a right preconditioner $\mathbf{M}[\theta]$ from the NGO, such that the condition number of $\mathbf{P} = \mathbf{C}\mathbf{M}^{-1}$ is much smaller than that of \mathbf{C} . The approach taken here loosely follows that of Pasetto et al. [30], in which a preconditioner for the time-varying diffusion is constructed from a reduced-order model. There, the discretised differential operator is restricted to a reduced bases, and the inverse of this coarse-scale

operator is taken as a starting point for a preconditioner. In our approach, both the reduced basis and the approximate solution operator on this basis are taken from the trained NGO.

For this example, we take the steady diffusion problems from the testing data set, formulate a finite difference discretization of the PDE, and use the data NGO trained in the previous section to construct a preconditioner. For the finite difference discretization, we assume a uniform grid (i.e. $\Delta x = \Delta y \equiv h$) and use a five-point difference scheme to approximate the differential operator:

$$\begin{aligned} -\nabla \cdot (\theta \nabla u) &= -\partial_x(\theta \partial_x u) - \partial_y(\theta \partial_y u), \\ [\partial_x(\theta \partial_x u)]_{i,j} &\approx \frac{1}{\Delta x} \left(\frac{\theta_{i,j} + \theta_{i+1,j}}{2} \frac{u_{i+1,j} - u_{i,j}}{\Delta x} - \frac{\theta_{i-1,j} + \theta_{i,j}}{2} \frac{u_{i,j} - u_{i-1,j}}{\Delta x} \right), \\ [\partial_y(\theta \partial_y u)]_{i,j} &\approx \frac{1}{\Delta y} \left(\frac{\theta_{i,j} + \theta_{i,j+1}}{2} \frac{u_{i,j+1} - u_{i,j}}{\Delta y} - \frac{\theta_{i,j-1} + \theta_{i,j}}{2} \frac{u_{i,j} - u_{i,j-1}}{\Delta y} \right), \end{aligned}$$

where $\theta_{i,j} = \theta(x_i, y_j)$ and $u_{i,j}$ is the finite-difference approximation to $u(x_i, x_j)$. We take $h = \frac{1}{99}$, which produces a discretisation with 100 points in the y -direction and 98 points in the x -direction (the Dirichlet boundary conditions imply that no boundary points need to be included). This produces a linear system $\mathbf{Cu} = \mathbf{b}$.

The linear system has $N = 9800$ unknowns, which is much larger than the $n = 144$ basis functions of the NGO. This means that we cannot directly apply the NGO as a preconditioner, since the NGO learns an operator of rank 144 at most. Applying it as a preconditioner directly would result in a singular system, which does not have a unique solution.

Nevertheless, we can use the trained NGO to construct a preconditioner \mathbf{M} such that $\kappa(\mathbf{CM}^{-1}) \ll \kappa(\mathbf{C})$. Generally, discretized differential operators may produce ill-conditioned matrices since they amplify high-frequency components while dampening low-frequency components. As such, a preconditioning strategy is to construct a preconditioner \mathbf{M} that amplifies the low frequencies, while preserving the high frequencies. To construct such a preconditioner, we first write the learned Green's function in a singular value decomposition (SVD) form.

Note that since the NGOs for the diffusion problem are of Galerkin form, i.e. with $\psi_m = \phi_m$, the separate test basis ψ_m is omitted here, and ϕ_m is used for both the test and trial bases.

1. For the given parameters θ , the NGO learns an approximation to the Green's operator as in (2.8):

$$\hat{G}[\theta](\mathbf{x}, \mathbf{x}') \approx \sum_{m,n} \phi_m(\mathbf{x}) \mathbf{A}_{mn}[\theta] \phi_n(\mathbf{x}'). \quad (4.17)$$

2. Now, we first orthonormalize the function basis: define the Gram matrix $\mathbf{G}_{mn} = \int_{\Omega} \psi_m(\mathbf{x}) \phi_n(\mathbf{x}) d\mathbf{x}$, and take the Cholesky decomposition $\mathbf{G} = \mathbf{L} \mathbf{L}^\top$. Then define $\tilde{\phi}_m(\mathbf{x}) = \sum_m \mathbf{L}_{mn}^{-1} \phi_n(\mathbf{x})$, which gives us a representation of the learned Green's function in terms of an orthonormal basis:

$$\hat{G}[\theta](\mathbf{x}, \mathbf{x}') \approx \sum_{m,n} \tilde{\phi}_m(\mathbf{x}) (\mathbf{L}^\top \mathbf{A}[\theta] \mathbf{L})_{mn} \tilde{\phi}_n(\mathbf{x}'). \quad (4.18)$$

3. Next, we compute an SVD of the inner matrix: $\mathbf{L}^\top \mathbf{A}[\theta] \mathbf{L} = \mathbf{U} \mathbf{\Sigma} \mathbf{V}^\top$, with \mathbf{U} and \mathbf{V} orthogonal matrices and $\mathbf{\Sigma} = \text{diag}(\sigma_1, \sigma_2, \dots, \sigma_n)$:

$$\hat{G}[\theta](\mathbf{x}, \mathbf{x}') \approx \sum_{m,n} \tilde{\phi}_m(\mathbf{x}) (\mathbf{U} \mathbf{\Sigma} \mathbf{V}^\top)_{mn} \tilde{\phi}_n(\mathbf{x}'). \quad (4.19)$$

We can then define two additional orthonormal bases, by merging the factors \mathbf{U} and \mathbf{V} into the basis

$\tilde{\phi}_m$:

$$\tilde{\phi}_n^{(U)} = \sum_m \tilde{\phi}_m \mathbf{U}_{mn}, \quad (4.20a)$$

$$\tilde{\phi}_n^{(V)} = \sum_m \tilde{\phi}_m \mathbf{V}_{mn}, \quad (4.20b)$$

$$\hat{G}[\theta](\mathbf{x}, \mathbf{x}') \approx \sum_m \tilde{\phi}_m^{(U)}(\mathbf{x}) \sigma_m \tilde{\phi}_m^{(V)}(\mathbf{x}'). \quad (4.20c)$$

Now, we focus on the orthonormal basis functions $\tilde{\phi}_i^{(U)}$: these are the left singular functions corresponding to the largest singular values of \hat{G} , and will therefore correspond to the *smallest* singular values of the differential operator \mathbf{C} . We now want a preconditioner that, when given a vector \mathbf{u} corresponding to a function $u(\mathbf{x})$, amplifies the low-frequency components in u that correspond to the basis functions $\tilde{\phi}_i^{(U)}$, while preserving the higher frequency components. For a function u , its decomposition into low and high frequencies is as follows:

$$u(\mathbf{x}) = \underbrace{\sum_i \langle \tilde{\phi}_i^{(U)}, u \rangle \tilde{\phi}_i^{(U)}(\mathbf{x})}_{\text{low frequencies}} + \underbrace{\left[u(\mathbf{x}) - \sum_i \langle \tilde{\phi}_i^{(U)}, u \rangle \tilde{\phi}_i^{(U)}(\mathbf{x}) \right]}_{\text{high frequencies}}, \quad (4.21)$$

where the orthonormality of the basis $\tilde{\phi}^{(U)}$ is crucial in making the separation easy to compute. To do this separation in the discrete setting, we sample the functions $\tilde{\phi}_i^{(U)}$, producing a matrix $\Phi \in \mathbb{R}^{N \times n}$, and replace the L^2 inner products in Ω by a quadrature rule with weights $\mathbf{W} \in \mathbb{R}^N$:

$$\mathbf{u} = \underbrace{\Phi \Phi^\top \text{diag}(W) \mathbf{u}}_{\text{low frequencies}} + \underbrace{[\mathbf{u} - \Phi \Phi^\top \text{diag}(W) \mathbf{u}]}_{\text{high frequencies}}. \quad (4.22)$$

Now, the preconditioner can amplify the low frequencies as $r \Phi \Sigma \Phi^\top \text{diag}(W) \mathbf{u}$: this amplifies each frequency proportionally to how strongly \mathbf{C} dampens that frequency, where the factor r remains to be chosen. If we add the high frequency components to this, we obtain a preconditioner:

$$\mathbf{M}^{-1} \mathbf{u} = \Phi \Sigma \Phi^\top \text{diag}(W) \mathbf{u} + r [\mathbf{u} - \Phi \Phi^\top \text{diag}(W) \mathbf{u}] = r \mathbf{u} + \Phi (\Sigma - r \mathcal{I}) \Phi^\top \text{diag}(W) \mathbf{u}. \quad (4.23)$$

In practice, it may not be the case that the NGO learns the first $n = 144$ modes accurately. Therefore, instead of taking all basis functions, we only take the first $k < n$ basis functions, resulting in the preconditioner:

$$\mathbf{M}_{k,r}^{-1} \mathbf{u} = r \mathbf{u} + \Phi_{:,1:k} (\Sigma_{1:k} - r \mathcal{I}) \Phi_{:,1:k}^\top \text{diag}(W) \mathbf{u}. \quad (4.24)$$

The value of r should now be such that the combined effect of the preconditioner and the differential operator, i.e. the matrix $\mathbf{C} \mathbf{M}^{-1}$, amplifies low frequencies and high frequencies approximately equally. One reasonable choice therefore is $r \propto \sigma_{k+1}$, which is the lowest amplification factor among the high frequencies. In the experiments in this section, we chose $r = \frac{\sigma_{k+1}}{2}$.

Note that the bulk of this process is independent of the resolution of the ‘full-order’ numerical scheme. Specifically, for an NGO with n basis functions preconditioning an $N \times N$ linear system, we can see the following:

- The orthogonalization of the basis requires only a Cholesky decomposition of an $n \times n$ matrix. In fact, if the basis ϕ_m has tensor structure (as is the case here), this can be factorized further. This step depends only on the basis, and is therefore independent of the parameters θ , meaning the decomposition only needs to be done once.
- The second expensive step is the SVD, which is performed on the matrix $\mathbf{L}^{-1} \mathbf{A} \mathbf{L}^{-\top}$, which is also $n \times n$.
- The preconditioner requires evaluating $\Phi^{(U)}$, which requires evaluating the basis functions on the N points (producing an $N \times n$ matrix) and multiplying by the $n \times n$ matrix $\mathbf{L}^{-\top} \mathbf{U}$.

- Finally, the resulting preconditioner, although it is $N \times N$ and dense, does not need to be stored in dense form since its action on a vector v can be computed easily:

$$\mathbf{M}^{-1}\mathbf{u} = r\mathbf{u} + \underbrace{\Phi^{(U)}_{N \times k} \left[(\Sigma - r\mathcal{I}) (\Phi^{(U)})^\top \text{diag}(W) \right]}_{k \times N} \mathbf{u}, \quad (4.25)$$

which means that after precomputing the two matrices indicated, $\mathbf{M}^{-1}\mathbf{u}$ can be computed in $\mathcal{O}(kN)$ time.

Since the NGO uses a certain function basis, the preconditioner only affects the components of the solution that lie in this basis, which are here associated with the low frequencies of the solution. This means that additional preconditioning can be introduced to accelerate convergence of the high-frequency components. One way this can be achieved is using multiplicative preconditioning, with a block-Jacobi preconditioner as a pre- and post-smoother. In this case, the combined preconditioner is expressed most naturally not as a matrix, but as a linear function $\mathbf{r} \mapsto \mathbf{u}^{(3)}$ comprised of the following three steps:

$$\mathbf{u}^{(1)} = \mathbf{M}_{\text{block-Jacobi}}^{-1} \mathbf{r}, \quad (4.26a)$$

$$\mathbf{u}^{(2)} = \mathbf{u}^{(1)} + \mathbf{M}_{\text{NGO}}^{-1} (\mathbf{r} - \mathbf{A}\mathbf{u}^{(1)}), \quad (4.26b)$$

$$\mathbf{u}^{(3)} = \mathbf{u}^{(2)} + \mathbf{M}_{\text{block-Jacobi}}^{-1} (\mathbf{r} - \mathbf{A}\mathbf{u}^{(2)}). \quad (4.26c)$$

Figure 12 shows the convergence behavior of GMRES. Here, the preconditioners were constructed from the data NGO trained in Section 4.3.1. For each of the preconditioner choices, 1000 test problems were discretized with finite differences and then solved with GMRES with a tolerance of 10^{-5} , with GMRES restarting every 20 iterations. This plot shows that using an NGO preconditioner greatly accelerates convergence compared to the un-preconditioned case, and also results in faster convergence than when using only a block-Jacobi preconditioner. However, the fastest convergence is obtained when both preconditioners are used in the way described above. Table 4 shows the mean number of GMRES iterations for different combinations of preconditioners, and the corresponding improvement over un-preconditioned GMRES. Note that the addition of an NGO preconditioner speeds up the convergence of GMRES by more than a factor 20, also when comparing the block-Jacobi preconditioner to the combined preconditioner.

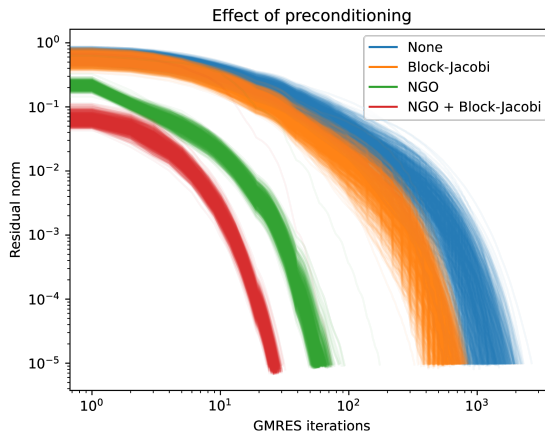


Figure 12: Convergence behavior of GMRES for 100×100 finite-difference discretizations of the diffusion equation, in four different cases: without any preconditioner, with block-Jacobi preconditioner, with NGO preconditioner, and with a combined preconditioner.

Table 4: Mean number of GMRES iterations required for convergence with different preconditioners.

Preconditioner	GMRES iterations	Improvement factor
None	1298	-
Block-Jacobi	599	2.2
NGO	62	20.9
NGO + block-Jacobi	29	44.5

5 Extension to Other Problems

5.1 Time-Dependent Diffusion

In this section we consider the time-dependent diffusion problem:

$$\begin{aligned} \left(\frac{\partial}{\partial t} - \nabla \cdot \theta \nabla \right) u &= f, \quad \forall (\mathbf{x}, t) \in \Omega \times \mathcal{T}, \\ \hat{\mathbf{n}} \cdot \theta \nabla u &= \eta, \quad \forall (\mathbf{x}, t) \in \Gamma_N \times \mathcal{T}, \\ \theta u &= g, \quad \forall (\mathbf{x}, t) \in \Gamma_D \times \mathcal{T}, \\ u &= u_0, \quad \forall (\mathbf{x}, t) \in \Omega \times \{0\}, \end{aligned} \quad (5.1)$$

where $\Omega = [0, L]^2$ and $\mathcal{T} = [0, T]$, which is a direct time-dependent generalization of the steady diffusion problem as treated in Section 4. The differences with respect to the static problem are that the operator in (5.1) contains a time derivative $\partial/\partial t$, the input functions θ , f , η and g are functions of space and time (\mathbf{x}, t) , and there is an initial condition $u = u_0$. Instead of resolving the Green's operator corresponding to (5.1) on the full time domain \mathcal{T} , we restrict ourselves to a time slab of length Δt , as shown in Figure 13. The solution to problem (5.1) can be expressed in terms of a Green's operator as

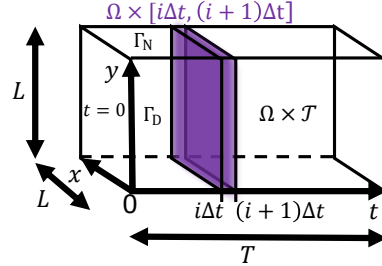


Figure 13: The space-time domain $\Omega \times \mathcal{T}$, with Neumann boundaries Γ_N on the top and bottom, Dirichlet boundaries Γ_D on the sides, and the initial condition boundary $t = 0$ on the left side.

$$\begin{aligned} u^{(i)}(\mathbf{x}, t) &= \int_{\Omega} G^{(i)}[\theta](i\Delta t) u^{(i-1)}(i\Delta t) d\mathbf{x}' + \int_{\Omega \times \Delta t_i} G^{(i)}[\theta] f d\mathbf{x}' dt' + \int_{\Gamma_N \times \Delta t_i} G^{(i)}[\theta] \eta d\mathbf{x}' dt' \\ &\quad - \int_{\Gamma_D \times \Delta t_i} g \hat{\mathbf{n}} \cdot \nabla G^{(i)}[\theta] d\mathbf{x}' dt', \end{aligned} \quad (5.2)$$

where $G^{(i)}$ is the Green's function corresponding to time slab i , and $u^{(0)}(0) = u_0$. The derivation of (5.2) is provided in Appendix A.2. By now stepping forward in time $u^{(i)} \rightarrow u^{(i+1)}$ from $t = 0$ to $t = T$, we resolve a piecewise continuous approximation of the true solution u over the full time domain \mathcal{T} .

5.1.1 NGO Architecture

Substitution of (2.8), where the basis functions $\psi_n^{(i)}$ and $\phi_m^{(i)}$ corresponding to time slab i are now functions of space and time (\mathbf{x}, t) , results in the NGO

$$\hat{u}^{(i)}(\mathbf{x}, t) = \hat{\mathcal{G}}^{(i)}[u^{(i-1)}, \theta, f, \eta, g](\mathbf{x}, t) = \hat{A}_{mn}^{(i)}(\mathbf{F}[\theta]) d_n^{(i)}[u^{(i-1)}, f, \eta, g] \phi_m^{(i)}(\mathbf{x}, t), \quad (5.3)$$

where

$$\begin{aligned} d_n^{(i)}[u^{(i-1)}, f, \eta, g] &= \int_{\Omega} \psi_n^{(i)}(i\Delta t) u^{(i-1)}(i\Delta t) d\mathbf{x}' + \int_{\Omega \times \Delta t_i} \psi_n^{(i)} f d\mathbf{x}' dt' + \int_{\Gamma_N \times \Delta t_i} \psi_n^{(i)} \eta d\mathbf{x}' dt' \\ &\quad - \int_{\Gamma_D \times \Delta t_i} g \hat{\mathbf{n}} \cdot \nabla \psi_n^{(i)} d\mathbf{x}' dt'. \end{aligned} \quad (5.4)$$

For model NGOs and data-free NGOs, the input $\mathbf{F}[\theta]$ is, as described in Section 3.1, the (unstabilized) system matrix

$$\begin{aligned} F_{nm}[\theta] &= \int_{\Omega \times \Delta t_i} \phi_m^{(i)} \mathcal{L}^*[\theta] \psi_n d\mathbf{x}' dt' - \int_{\Gamma \setminus \Gamma_N \times \Delta t_i} \theta \psi_n \hat{\mathbf{n}} \cdot \nabla \phi_m^{(i)} d\mathbf{x}' dt' + \int_{\Gamma \setminus \Gamma_D \times \Delta t_i} \theta \phi_m^{(i)} \hat{\mathbf{n}} \cdot \nabla \psi_n d\mathbf{x}' dt' \\ &\quad + \int_{\Omega} \psi_n((i+1)\Delta t) \phi_m^{(i)}((i+1)\Delta t) d\mathbf{x}', \end{aligned} \quad (5.5)$$

which is equivalent to Equation A.11. For data NGOs, $\mathbf{F}[\theta]$ is the material parameter θ integrated against the test basis as

$$F_n[\theta] = \int_{\Omega \times \Delta t_i} \psi_n \theta d\mathbf{x}' dt'. \quad (5.6)$$

To data NGOs, we also provide the additional input $F_{t,n} \equiv \int_{\Omega} \psi_n((i+1)\Delta t) d\mathbf{x}'$, for the reason explained in Section C.2. We use basis functions $\psi(\mathbf{x}, t) \equiv \{\psi_n(\mathbf{x}, t)\}_{n=1}^N$ and $\phi(\mathbf{x}, t) \equiv \{\phi_m(\mathbf{x}, t)\}_{m=1}^N$, which are Kronecker outer products of 1D basis functions such as

$$\phi(\mathbf{x}, t) = \phi^{(t)}(t) \otimes_{\mathbf{K}} \phi^{(x)}(x) \otimes_{\mathbf{K}} \phi^{(y)}(y), \quad (5.7)$$

where $\phi^{x_i}(x_i) \equiv \{\phi_l^{x_i}(x_i)\}_{l=1}^{n_i}$, n_i is the number of basis functions in dimension i , and $\otimes_{\mathbf{K}}$ is the Kronecker product. In Appendix F, we show how to exploit the Kronecker product structure of the basis to enable more time and memory efficient assembly of the system matrix for model NGOs and data-free NGOs. If we now substitute

$$u^{(i-1)}(i\Delta t) = u_m^{(i-1)} \phi_m^{(i-1)}(i\Delta t), \quad (5.8)$$

into (5.4), we end up with the time stepping scheme

$$\hat{\mathbf{u}}^{(i)} = \hat{\mathbf{A}}^{(i)} \mathbf{d}^{(i)} = \hat{\mathbf{A}}^{(i)} \mathbf{M}_{lr} \hat{\mathbf{u}}^{(i-1)} + \hat{\mathbf{A}}^{(i)} \mathbf{d}_{\mathbf{x}}^{(i)}, \quad (5.9)$$

where we define

$$M_{lr,nm} \equiv \int_{\Omega} \psi_n^{(i)}(i\Delta t) \phi_m^{(i-1)}(i\Delta t) d\mathbf{x}' = \int_{\Omega} \psi_n^{(i)}(i\Delta t) \phi_m^{(i)}((i+1)\Delta t) d\mathbf{x}', \quad (5.10)$$

as the mass matrix corresponding to the basis functions evaluated at the left and right ends of the time step element, and

$$d_{\mathbf{x},n}^{(i)}[f, \eta, g] \equiv d_n^{(i)}[u^{(i-1)}, f, \eta, g] - \int_{\Omega} \psi_n^{(i)}(\Delta t_i) u^{(i-1)}(\Delta t_i) d\mathbf{x}' \quad (5.11)$$

as the right-hand-side vector corresponding to the forcing and boundary condition terms. To summarize, the architectures of the NGOs that are used for the steady diffusion problem (treated in Section 3) can be used to predict a single timestep forward in time for the time-dependent diffusion problem, if one accounts for the additional dependence of the basis functions on time t , and the additional input u^{i-1} (and a few other details, which are discussed in Appendix C.2). The resulting model can then be used to march forward in time using Equation 5.9. In practice, we define the basis $\phi^{(t)}(t)$ only on a single element in time and shift this basis forward in time upon doing time steps, which is equivalent to a discontinuous basis in time. In the remainder of this section, we investigate methods to preserve key properties of solutions to Equation (5.1) that enable an NGO trained on a single time-step to predict solutions autoregressively over an arbitrary number of time steps.

5.1.2 Inductive Bias: Time Stepping Stability

To study the stability over time of the solution of the time-dependent diffusion problem, we assume a Galerkin discretization with $\psi(\mathbf{x}, t) = \phi(\mathbf{x}, t)$ and substitute the solution u as test function v into the weak form (Equation A.10), which results in the energy equation

$$\begin{aligned}\Delta E^{(i)} &\equiv \frac{1}{2} \int_{\Omega} \left(u^{(i)} \right)^2 ((i+1)\Delta t) d\mathbf{x}' - \frac{1}{2} \int_{\Omega} \left(u^{(i-1)} \right)^2 (i\Delta t) d\mathbf{x}' \\ &= -D^{(i)}[\theta][u^{(i)}, u^{(i)}] + \int_{\Omega \times \Delta t_i} u^{(i)} f d\mathbf{x}' dt' + \int_{\Gamma_N \times \Delta t_i} u^{(i)} \eta d\mathbf{x}' dt' \\ &\quad + \int_{\Gamma_D \times \Delta t_i} g (C_s - \hat{\mathbf{n}} \cdot \nabla) u^{(i)} d\mathbf{x}' dt'\end{aligned}\quad (5.12)$$

where

$$\begin{aligned}D^{(i)}[\theta][u^{(i)}, u^{(i)}] &= \int_{\Omega \times \Delta t_i} \theta \left\| \nabla u^{(i)} \right\|_2^2 d\mathbf{x}' dt' + \int_{\Gamma_D \times \Delta t_i} \theta u^{(i)} (C_s - 2\hat{\mathbf{n}} \cdot \nabla) u^{(i)} d\mathbf{x}' dt' \\ &\geq \alpha^{(i)}[\theta] \left\| u^{(i)} \right\|^2\end{aligned}\quad (5.13)$$

is the diffusive energy/entropy dissipation, the second right-hand-side term is the energy production, and the third and fourth terms are energy outflow on the Neumann and Dirichlet boundaries, respectively. C_s is a Nitsche stabilization constant [31], which is required to ensure non-negativity of D . Substituting $u^{(i)} = u_m^{(i)} \phi_m^{(i)}$ in (5.13) results in the corresponding discrete energy dissipation relation

$$\frac{1}{2} \left\| \mathbf{u}^{(i)} \right\|_{\mathbf{M}_{rr}}^2 - \frac{1}{2} \left\| \mathbf{u}^{(i-1)} \right\|_{\mathbf{M}_{rr}}^2 \leq \left(\mathbf{u}^{(i)} \right)^T \mathbf{h}_x^{(i)}, \quad (5.14)$$

where $\mathbf{u}^{(i)} = \{u_m^{(i)}\}_{m=1}^N$,

$$\mathbf{h}_x^{(i)} = \int_{\Omega \times \Delta t_i} \phi^{(i)} f d\mathbf{x}' dt' + \int_{\Gamma_N \times \Delta t_i} \phi^{(i)} \eta d\mathbf{x}' dt' + \int_{\Gamma_D \times \Delta t_i} g (C_s - \hat{\mathbf{n}} \cdot \nabla) \phi^{(i)} d\mathbf{x}' dt' \quad (5.15)$$

and $\left\| \cdot \right\|_{\mathbf{M}_{rr}}$ is the vector norm induced by the mass matrix

$$M_{rr, nm} \equiv M_{rr, nm}^{(i)} = \int_{\Omega} \phi_n^{(i)} ((i+1)\Delta t) \phi_m^{(i)} ((i+1)\Delta t) d\mathbf{x}' \quad (5.16)$$

corresponding to the basis functions evaluated at the end of the time step. The discrete energy equation (5.14) describes the evolution of the L^2 norm (in space) of the discrete solution $u^{(i)} = u_m^{(i)} \phi_m^{(i)}$ over time.

Operator Stability To derive a stability criterion for the output of the system network from (5.14), we consider, without loss of generality, the homogeneous counterpart of (5.1) where $f = \eta = g = 0$. In the homogeneous setting, the discrete energy inequality (5.14) simplifies to

$$\frac{1}{2} \left\| \mathbf{u}^{(i)} \right\|_{\mathbf{M}_{rr}}^2 - \frac{1}{2} \left\| \mathbf{u}^{(i-1)} \right\|_{\mathbf{M}_{rr}}^2 \leq 0. \quad (5.17)$$

Substitution of the time stepping scheme (5.9) (with $\mathbf{d}_{\mathbf{x}}^{(i)} = 0$) into Equation (5.17) (with $\mathbf{h}_x^{(i)} = 0$) and reordering gives

$$\frac{\left\| \hat{\mathbf{A}}^{(i)}[\theta] \mathbf{M}_{lr} \mathbf{u}^{(i-1)} \right\|_{\mathbf{M}_{rr}}}{\left\| \mathbf{u}^{(i-1)} \right\|_{\mathbf{M}_{rr}}} \leq 1. \quad (5.18)$$

Since (5.18) is true for all $\mathbf{u}^{(i-1)}$, it implies the stability criterion

$$\sup_{\mathbf{u}^{(i-1)}} \frac{\left\| \hat{\mathbf{A}}^{(i)}[\theta] \mathbf{M}_{lr} \mathbf{u}^{(i-1)} \right\|_{\mathbf{M}_{rr}}}{\left\| \mathbf{u}^{(i-1)} \right\|_{\mathbf{M}_{rr}}} \equiv \left\| \hat{\mathbf{A}}^{(i)}[\theta] \mathbf{M}_{lr} \right\|_{\mathbf{M}_{rr}} \leq 1 \quad (5.19)$$

To guarantee stability of the NGOs, we therefore need to ensure that NGOs produce matrices $\hat{\mathbf{A}}^{(i)}[\theta]$ that satisfy the criterion (5.19). Note that (5.19) is a property of the matrix $\hat{\mathbf{A}}^{(i)}[\theta]$ that is independent of f , η and g , so (5.19) is also true for the inhomogeneous problem.

To ensure that output of the system network in model and data-free NGOs are dissipative in the sense of (5.19), we rely on a preconditioned system network, as described in Section 4.2, where \mathbf{F}_0 incorporates stabilization using Nitsche's method [31] guaranteeing that \mathbf{F}_0^{-1} satisfies (5.19). For data NGOs, however, we assume the PDE information to be unknown and, thus, the system matrix to be unavailable. To ensure that a data NGO satisfies (5.19) we propose a matrix norm scaling layer:

$$\hat{\mathbf{A}}'^{(i)} = \begin{cases} \hat{\mathbf{A}}^{(i)} & \|\hat{\mathbf{A}}^{(i)}\mathbf{M}_{lr}\|_{\mathbf{M}_{rr}} \leq S, \\ \frac{S}{\|\hat{\mathbf{A}}^{(i)}\mathbf{M}_{lr}\|_{\mathbf{M}_{rr}}} \hat{\mathbf{A}}^{(i)} & \|\hat{\mathbf{A}}^{(i)}\mathbf{M}_{lr}\|_{\mathbf{M}_{rr}} > S, \end{cases} \quad (5.20)$$

which guarantees that

$$\|\hat{\mathbf{A}}^{(i)}\mathbf{M}_{lr}\|_{\mathbf{M}_{rr}} \leq S \leq 1. \quad (5.21)$$

Here, $S \leq 1$ is a hyperparameter that determines the maximum norm that the data NGO is allowed to predict. That is, if the output of the system network $\hat{\mathbf{A}}^{(i)}$ is such that it violates (5.19), we scale it back, such that the resulting scaled matrix $\hat{\mathbf{A}}'^{(i)}$ does satisfy (5.19). For computational reasons, we do not explicitly calculate $\|\hat{\mathbf{A}}^{(i)}\mathbf{M}_{lr}\|_{\mathbf{M}_{rr}}$, but we estimate it up to relative error tolerance $\epsilon = 10^{-3}$ using a power iteration algorithm [32], of which implementation details can be found in Appendix D.2.

In Figure 14, we show the effect of the preconditioning strategy and the norm scaling layer on the mass-matrix-generalized eigenvalue spectrum and long term stability of a model NGO and data NGO, respectively. Details of the model architectures are highlighted in Appendix C.2. The models have been trained on dataset D, described in Appendix B.2, using the training procedure described in Appendix D.2. In Figure 14(a), we show that the preconditioning strategy for the model NGO and the norm scaling layer (5.20) for the data NGO ensure that both models satisfy (5.19). The \mathbf{M}_{rr} -generalized eigenvalue spectrum of the model NGO also visually overlaps with the stabilized FEM spectrum. In Figure 14(b), we show that the included inductive biases ensure that both models have time integration errors that remain stable over time for 1000 time steps of size $\Delta t/T = 10^{-3}$, even though both NGOs have been trained on a single time step of size $\Delta t = 10^{-3}$ only. We observed that choosing a conservative $S < 1$ (we chose 0.8) results in lower error

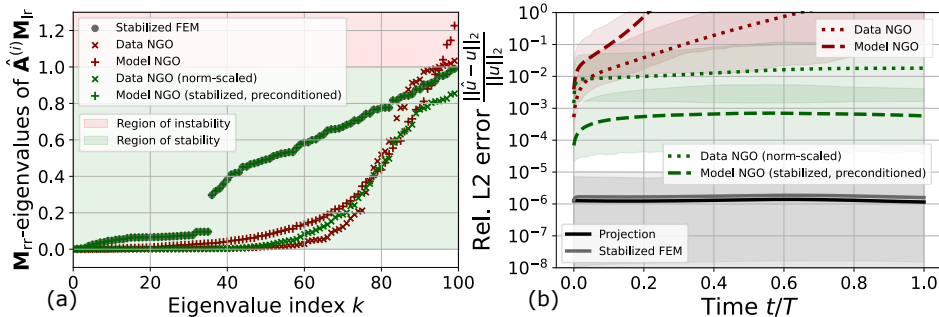


Figure 14: Effect of adding the Nitsche-stabilized Neumann series preconditioning to a model NGO, and the norm scaling layer (5.20) to a data NGO, on their (a) mass matrix \mathbf{M}_{rr} -generalized eigenvalue spectrum and (b) relative time step L^2 test error over time. Projection and stabilized FEM are included as reference in black and gray, respectively. In (a), points correspond to the spectrum of a single matrix corresponding to a manufactured θ (manufactured as in dataset D). In (b), lines and shaded areas are, respectively, 95% confidence intervals on 100 manufactured solutions generated in the same way as dataset D, but with $\lambda/L = \tau/T = 1$.

accumulation.

Conservation and Dissipation Laws In the remainder of this section we explore the effect of controlling the errors in the laws of mass conservation (derived by setting $v = 1$ in (A.10) and $u^{(i)} = u_m^{(i)} \phi_m^{(i)}$),

$$\begin{aligned}\Delta m^{(i)} &\equiv u_m^{(i)} \int_{\Omega} \phi_m^{(i)}((i+1)\Delta t) d\mathbf{x}' - u_m^{(i-1)} \cdot \int_{\Omega} \phi_m^{(i-1)}(i\Delta t) d\mathbf{x}' \\ &= \int_{\Omega \times \Delta t_i} f d\mathbf{x}' dt' + \int_{\Gamma_N \times \Delta t_i} \eta d\mathbf{x}' dt' + u_m^{(i)} \int_{\Gamma \setminus \Gamma_N \times \Delta t_i} \theta \hat{\mathbf{n}} \cdot \nabla \phi_m^{(i)} d\mathbf{x}' dt',\end{aligned}\quad (5.22)$$

and energy dissipation (5.14) on the accuracy of the predictions of NGOs of solutions (5.1) over time. Collecting (5.22) and (5.14) we obtain a system of equations for the vector of unknowns $\mathbf{u}^{(i)}$ given by

$$\begin{cases} \left(\mathbf{u}^{(i)}\right)^T \mathbf{c}^{(i)} = C^{(i)} & \text{(mass),} \\ \frac{1}{2} \left\| \mathbf{u}^{(i)} \right\|_{\mathbf{M}_{rr}}^2 - \frac{1}{2} \left\| \mathbf{u}^{(i-1)} \right\|_{\mathbf{M}_{rr}}^2 \leq \left(\mathbf{u}^{(i)}\right)^T \mathbf{h}_x^{(i)} & \text{(energy),} \end{cases}\quad (5.23)$$

where we defined

$$c_m^{(i)}[\theta] = \int_{\Omega} \phi_m^{(i)}((i+1)\Delta t) d\mathbf{x}' - \int_{\Gamma \setminus \Gamma_N} \theta \hat{\mathbf{n}} \cdot \nabla \phi_m^{(i)} d\mathbf{x}' dt' \quad (5.24)$$

and

$$C^{(i)}[u^{(i-1)}, f, \eta] = \int_{\Omega} u_m^{(i-1)} \phi_m^{(i-1)}(i\Delta t) d\mathbf{x}' + \int_{\Omega \times \Delta t_i} f d\mathbf{x}' dt' + \int_{\Gamma_N \times \Delta t_i} \eta d\mathbf{x}' dt'. \quad (5.25)$$

To control the error in the output $\hat{\mathbf{u}}^{(i)}$ of an NGO with respect to the relations in (5.23) we apply the following correction

$$\hat{\mathbf{u}}'^{(i)} = a \hat{\mathbf{u}}^{(i)} + b \mathbf{c}^{(i)}, \quad (5.26)$$

where a and b are scalars. Substitution of (5.26) into (5.23) results in a quadratic system of equations that can be solved for a and b . Algorithmically, we start with $a = 1$ and correct only the mass conservation equation by solving for b . We then check for violation of the energy inequality, and if violated, we do another correction on top of the first correction, in which we solve for $a < 1$ and b simultaneously.

In Figure (15), we show the effect of adding the correction in (5.26) to a data NGO on its errors in the predicted mass $m(t) = \int_{\Omega} u(\mathbf{x}, t) d\mathbf{x}$ and energy $E(t) = 1/2 \int_{\Omega} u^2(\mathbf{x}, t) d\mathbf{x}$ over time. Details of the model

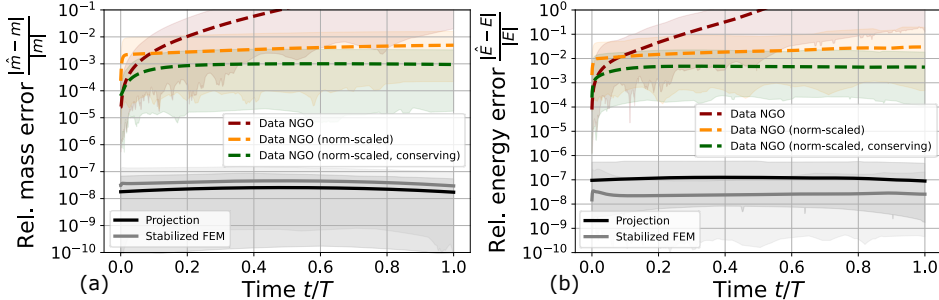


Figure 15: Effect of adding the conservation correction (5.26) to a data NGO on the errors of its predicted (a) $m(t) = \int_{\Omega} u(\mathbf{x}, t) d\mathbf{x}$ and (b) energy $E(t) = 1/2 \int_{\Omega} u^2(\mathbf{x}, t) d\mathbf{x}$ over time. Projection and stabilized FEM are included as reference in black and gray, respectively. All models are trained on dataset D (Appendix B). Lines and shaded areas are, respectively, averages and 95% confidence intervals on 100 manufactured solutions generated in the same way as dataset D, but with $\lambda/L = \tau/T = 1$.

architectures are highlighted in Appendix C.2. The models have been trained on dataset D, described in Appendix B.2, using the training procedure described in Appendix D.2. While it can be observed in Figures (15) (a) and (b) that the correction (5.26) gives an improvement in the error of the predicted mass $\hat{m}(t)$ and energy $\hat{E}(t)$ over time, with respect to $m(t)$ and $E(t)$, respectively, it does not eliminate such errors. Such a discrepancy is due to the fact the correction in (5.26) only gives us control over the equality in the mass

conservation equation of (5.23), but not over the magnitudes of the different contributions, and only ensures the satisfaction of an inequality in the energy dissipation relation of (5.23) which may be inexact.

Finally, Figure (16) shows that incorporating the mass and energy relations in (5.23) through the correction (5.26) to a data NGO results in an overall lower solution errors over time.

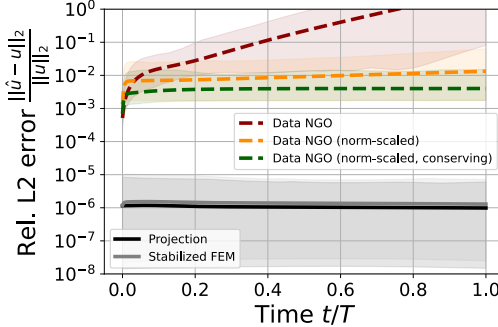


Figure 16: Effect of adding the conservation correction (5.26) to a data NGO. Projection and stabilized FEM are included as reference in black and gray, respectively. All models are trained on dataset D (Appendix B). Lines and shaded areas are, respectively, averages and 95% confidence intervals on 100 manufactured solutions generated in the same way as dataset D, but with $\lambda/L = \tau/T = 1$.

5.1.3 Results

In this section, we perform the same test as considered in Figure 8, except that here, we compare NGOs to other neural operators in their generalization across test data length as well as time scales. Additionally, we compare the long term stability of NGOs against the same models from literature. The architectural details of the used models are essentially identical to those corresponding to Figure 8, except that the models now also use quadrature and basis functions in space-time. Specifically, the DeepONet, VarMiON, data NGO, data-free NGO and model NGO now use a 2 linear \times 10 cubic \times 10 cubic B-spline basis in space-time (t, x, y) and all models use a quadrature grid of approximately $2 \times 100 \times 100$ points. The FNO uses $2 \times 10 \times 10$ Fourier modes, and the standalone NN (U-Net) uses 3-dimensional convolutions. The VarMiON is now limited to using only $2 \times 5 \times 5$ uniform quadrature points, because of the limited parameter budget of $3 \cdot 10^4$ trainable parameters. Details of the model architectures are highlighted in Appendix C.2. The models have been trained on dataset D, described in Appendix B.2, using the training procedure described in Appendix D.2.

Generalization Error Across Length and Time Scales In Figure 17, the single timestep accuracies of the different NOs are compared on test datasets with varying GRF time and length scales τ and λ . The models are tested on in-distribution time and length scales $0.5 < \tau/T < 1$, $0.5 < \lambda/L < 1$, (dataset D), as well as on out-of-distribution test data with finer scales $0.05 < \tau/T < 0.5$, $0.05 < \lambda/L < 0.5$ (generated in the same way as dataset D). Observations are similar to those in Figure 8 for the steady diffusion problem: the model NGO is the most accurate, followed by the data-free NGO. This is the case in the test with varying length scale as well as in the test with varying time scale, on large scale in-distribution data, as well as on fine scale out-of-distribution data. A difference with respect to the steady diffusion results presented in Figure 8 is that the data NGO has slightly higher errors. The explanation is that we needed to compromise on single timestep accuracy, in order to achieve long-term stability. We observed that choosing a smaller, more conservative norm clipping value $S < 1$ resulted in less error accumulation, and therefore, we chose $S = 0.8$. However, $S = 0.8$ is far off from the value $S \approx 0.99$ that agrees with the true data, which explains the higher single timestep error of the data NGO.

Stability of Different NOs Over Time Figure 18 shows a comparison of the errors over time of the same set of models as presented in Figure 17. In Figure 18(a), the models are tested on a set of 100 different in-distribution problems with large time and length scales $\tau/T = \lambda/L = 1$. Note that the single timestep error (Figure 17) only determines the model error after the first timestep: a lower single timestep error

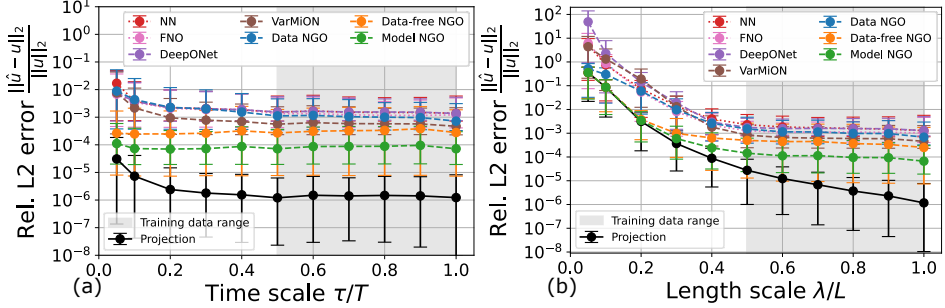


Figure 17: Single time step relative L^2 test error versus (a) time scale τ/T and (b) length scale λ/L for a bare NN (here a U-Net), and the same NN, when used in a DeepONet, VarMiON, data NGO, data-free NGO and model NGO. All models have roughly $3 \cdot 10^4$ trainable parameters, and all models (except the NN and FNO) use the same $2 \text{ linear} \times 10 \text{ cubic} \times 10 \text{ cubic}$ B-spline basis in space-time (t, x, y) . Points and error bars are, respectively, averages and 95% confidence intervals on 1000 manufactured solutions generated in the same way as dataset D, but with $\lambda/L = 1$ (in (a)) and with $\tau/T = 1$ (in (b)).

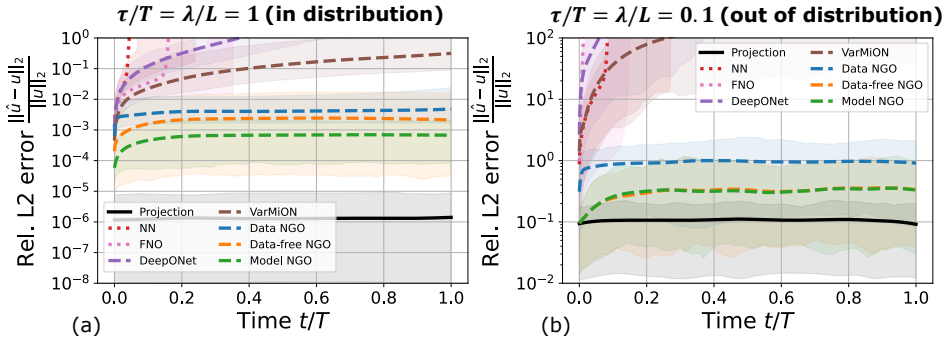


Figure 18: Relative time step L^2 test error over time on (a) in distribution data with time and length scale $\tau/T = \lambda/L = 1$ and (b) out of distribution data with $\tau/T = \lambda/L = 0.1$, for a bare NN (here a U-Net), and the same NN, when used in a DeepONet, VarMiON, data NGO, data-free NGO and model NGO (an FNO is also added for comparison). All models have roughly $3 \cdot 10^4$ trainable parameters, and all models (except the NN and FNO) use the same $2 \text{ linear} \times 10 \text{ cubic} \times 10 \text{ cubic}$ B-spline basis, and are thus limited by the same L^2 projection error lower bound, indicated in black. Points and shaded areas are, respectively, averages and 95% confidence intervals on 100 manufactured solutions generated in the same way as dataset D, but with $\tau/T = \lambda/L = 1$ (in (a)) and with $\tau/T = \lambda/L = 0.1$ (in (b)).

does not necessarily imply less accumulation of error over time. Only the NGOs manage to keep their errors finite over time, which demonstrates the effectiveness of the additional inductive bias that the Green's formulation of the NGO allows us to introduce. In Figure 18(b), we test the same models on 100 far out-of-distribution problems with time and length scales $\tau/T = \lambda/L = 0.1$. While the best approximation in the space deteriorates in the presence of such fine scales in the data, the results do demonstrate the reliability of the NGOs, provided by the additional inductive bias, in far out-of-distribution conditions.

5.2 Advection-Diffusion

The final test case we consider is the advection-diffusion equation with inhomogeneous Dirichlet and Neumann boundary conditions:

$$\begin{cases} -\nabla \cdot (\theta \nabla u) + \mathbf{c} \cdot \nabla u = f & \text{on } \Omega = (0, 1)^2, \\ \theta \nabla u \cdot \mathbf{n} - (\mathbf{c} \cdot \mathbf{n})_- u = \eta & \text{on } \Gamma_N = (0, 1) \times \{0, 1\}, \\ \theta u = g & \text{on } \Gamma_D = \{0, 1\} \times (0, 1), \end{cases} \quad (5.27)$$

where $(\mathbf{c} \cdot \mathbf{n})_- = \min(\mathbf{c} \cdot \mathbf{n}, 0)$. Compared to the pure diffusion equation, the advection-diffusion equation presents a more challenging problem due to a number of factors. First, the solution now depends non-linearly

on both the diffusion θ and the velocity field \mathbf{c} . Second, for large Péclet numbers (the ratio between the advection \mathbf{c} and the diffusion θ) the true solution will feature boundary layers near the Dirichlet boundaries, which may be difficult to resolve. Note that the boundary condition $\theta \nabla u \cdot \mathbf{n} - (\mathbf{c} \cdot \mathbf{n})_- u = \eta$ differs from the Neumann boundary condition on the inflow part of the top and bottom boundaries (i.e. where $\mathbf{c} \cdot \mathbf{n} < 0$). This change was made to facilitate stable finite element discretizations.

Figure 19 shows five problems from the advection-diffusion data set. Note that the varying direction and magnitude of the velocity field means that different problems lead to boundary layers of varying strengths and near different parts of the boundary.

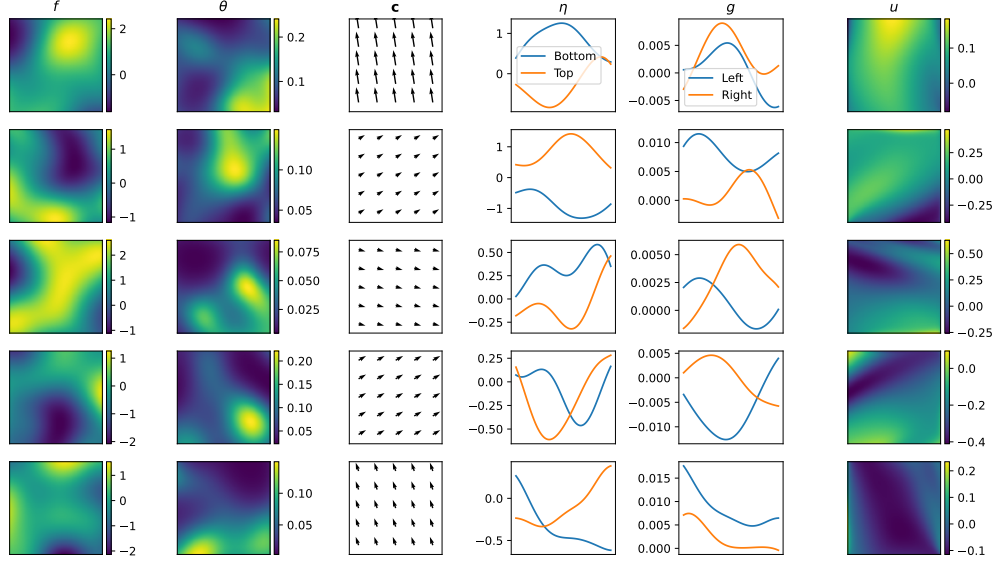


Figure 19: Five example problems and solutions from the advection-diffusion data set.

5.2.1 NGO architectures

The architectures of the NGOs are largely unchanged from their architectures in Section 4.3.1. The differences are listed in Appendix C.3. Regarding the training procedure, all relevant parameters are still as given in Table 14, with the exception of the out-of-distribution training data, which is now absent.

5.2.2 Results

Table 5 shows the training and testing error of the data NGO, model NGO, and FNO on the advection-diffusion data. For reference, the table also includes the SUPG, Galerkin and L^2 projection errors, both using the same cubic B-spline basis as the NGOs. The table also lists the accuracy of POD-Galerkin, a simple reduced basis method that produces excellent results for the pure diffusion equation (see Table 2). For advection-diffusion, POD-Galerkin produces worse results due to the fact that Galerkin methods are generally unsuitable for advection-dominated problems.

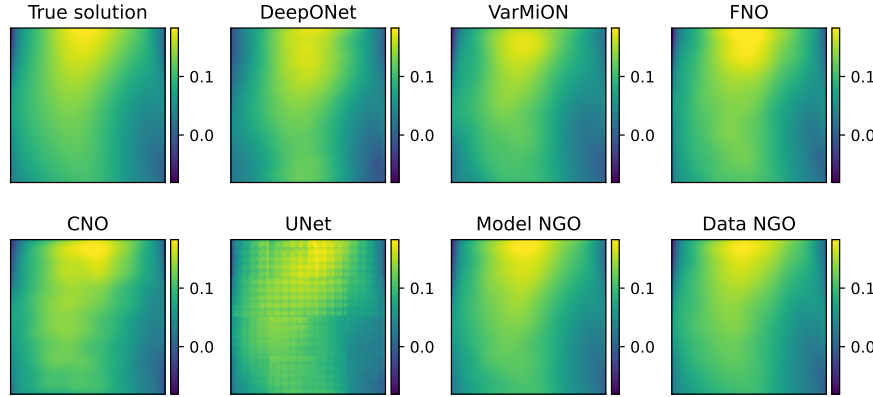
Figure 20 shows the true solution alongside the solution predictions made by the different model architectures for one problem from the training data, and one from the testing data.

To highlight the computational efficiency of the different models we show the time and memory requirements of CNOs, FNOs, and NGOs per batch of 100 inputs in Table 6. From these results, it is clear that NGOs require more time and less memory to train than U-Nets and VarMiONs, but less than CNOs and FNOs.

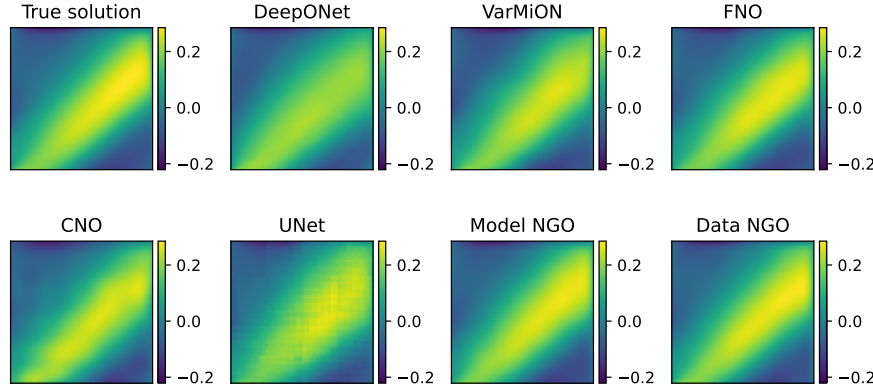
To illustrate the scaling of the error with the data-set size we show in Figure 21 the effect that the amount of training data has on the model accuracy for FNOs, CNOs, data NGOs, and model NGOs. As the plot

Table 5: Errors (in terms of mean and standard deviation) of different model architectures on the advection diffusion data set.

Model	Parameters	Test error	
		Training set	Testing set
DeepONet	36819	$32.52\% \pm 15.46\%$	$33.30\% \pm 19.52\%$
VarMiON	32233	$12.21\% \pm 7.16\%$	$12.30\% \pm 6.89\%$
FNO	31817	$8.95\% \pm 2.72\%$	$11.49\% \pm 5.80\%$
CNO	29837	$15.43\% \pm 6.46\%$	$21.23\% \pm 10.30\%$
U-Net	31721	$17.88\% \pm 6.85\%$	$18.02\% \pm 7.29\%$
Data NGO	28021	$6.82\% \pm 3.26\%$	$7.66\% \pm 3.99\%$
Model NGO	28387	$7.06\% \pm 3.34\%$	$7.98\% \pm 4.11\%$
Galerkin		$14.13\% \pm 12.46\%$	$14.57\% \pm 14.10\%$
SUPG		$6.93\% \pm 5.92\%$	$7.00\% \pm 6.21\%$
Projection		$3.99\% \pm 3.43\%$	$4.06\% \pm 3.66\%$
POD-Galerkin		$30.42\% \pm 19.25\%$	$29.16\% \pm 16.52\%$



(a) The true solution of one problem from the training data set, and model predictions of the different neural operators.



(b) The true solution of one problem from the testing data set, and model predictions of the different neural operators.

Figure 20: The true solution and model predictions to one problem from the training data set (Figure 20a) and one problem from the testing data set (Figure 20b)

Table 6: Performance comparison, in terms of time and memory usage, of NGOs compared to other models.

Model	Computing time per batch [ms]	Peak memory usage [MB]
Model NGO	9.3	522
Data NGO	6.1	347
VarMiON	3.6	87
FNO	107.3	4201
CNO	43.2	880
U-Net	5.6	260

shows, both NGO models outperform the other models for each tested data set size, although the difference becomes small for large data sets.

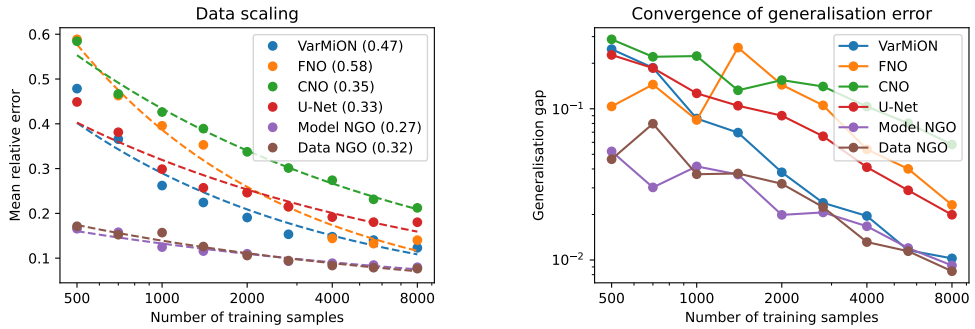


Figure 21: Left: mean relative error of VarMiON, FNO, CNO, U-Net, model NGO, and data NGO, each for varying amounts of training data. The fitted curves are of the form $\text{err} = a \cdot N^{-r}$. The exponent r is listed in parentheses for each model. Right: the generalization gap, i.e. the difference between the testing error and the training error, for varying amounts of training data.

6 Conclusion

In this work, we have introduced the Neural Green’s Operator, a machine learning architecture for learning the solution operator to parametric families of linear PDEs. Our construction of NGOs is based on a finite-dimensional representation of Green’s functions. Such a representation enables the preservation of the linear action of Green’s operators on the inhomogeneity fields, while approximating the nonlinear dependence of the Green’s function on the coefficients of the PDE using neural networks that take weighted averages of such coefficients as input. This construction reduces the complexity of the problem from learning the entire solution operator and its dependence on all parameters to only learning the Green’s function and its dependence on the PDE coefficients. Moreover, taking weighted averages, rather than point samples, of input functions decouples the network size from the number of sampling points, enabling efficient resolution of multiple scales in the input fields. We distinguished three use cases of NGOs: the model NGO, which is used when the underlying PDE is known and training data is available; the data-free NGO, which is used when the underlying PDE is known, but training data is unavailable; and the data NGO, which is used when training data is available, but the model that underlies the data is unknown. For the steady diffusion problem, the accuracy of NGOs exceeds that of VarMiONs, DeepONets, and FNOs, particularly when testing models on finer-scale data that do not lie in the training distribution. Similar trends were observed for the time-dependent diffusion problem and the advection-diffusion problem.

A key distinguishing feature of NGOs is that, in addition to predicting the solutions of parametric PDEs, they return explicit representations of the parametric Green’s functions of such PDEs. We demonstrated that an explicit representation of the Green’s function enables the induction of biases in the network, such as preconditioning the output of the system network and the incorporation of conservation and dissipation

laws, leading to improved accuracy of the predicted solutions. The efficacy of such inductive biases was demonstrated in the time-dependent diffusion problem, which allowed us to embed operator stability ensuring long-term autoregressive rollout and thereby pointwise accuracy in time, even when trained on a single time step. Furthermore, we demonstrated that Green's functions inferred by NGOs can be used to construct effective matrix preconditioners for accelerating iterative solvers of large-scale problems.

Although we provide a proof of concept for the use of NGOs as solution operators for linear PDEs, several research directions emerge from this work. One research direction includes enriching the space of parameters that are encoded in NGOs to solve PDEs in more general settings. Such settings can include varying geometries of the problem domain, as well as varying the type of boundary condition applied on the boundary segments. Another direction of research involves the customized use of NGOs to accelerate other algorithms. Of particular interest is the iterative use of NGOs within a fixed-point algorithm, such as Newton, to solve nonlinear problems, as well as the extension of the matrix preconditioning strategies for accelerating iterative solvers and time integration strategies for accelerating transient solvers. Lastly, we are also interested in exploring training strategies that would lead to even more accurate models.

Code corresponding to the steady diffusion problem is available at <https://github.com/JoostHMPriins/ngo>.

References

- [1] T.J.R. Hughes, G.R. Feij  o, L. Mazzei, and J. Quincy. The variational multiscale method—a paradigm for computational mechanics. *Computer Methods in Applied Mechanics and Engineering*, 166(1-2):3–24, 1998.
- [2] T.J.R. Hughes. *The finite element method: linear static and dynamic finite element analysis*. Courier Corporation, 2012.
- [3] J.D. Anderson and J. Wendt. *Computational fluid dynamics*. Springer, 1995.
- [4] Y. Bazilevs, K. Takizawa, and T.E. Tezduyar. *Computational fluid-structure interaction: methods and applications*. John Wiley & Sons, 2013.
- [5] Y. Fung, P. Tong, and X. Chen. *Classical and computational solid mechanics*. World Scientific, 2001.
- [6] L. Lu, X. Meng, S. Cai, Z. Mao, S. Goswami, Z. Zhang, and G.E. Karniadakis. A comprehensive and fair comparison of two neural operators (with practical extensions) based on fair data. *Computer Methods in Applied Mechanics and Engineering*, 393:114778, 2022.
- [7] K. Hornik, M. Stinchcombe, and H. White. Multilayer feedforward networks are universal approximators. *Neural Networks*, 2(5):359–366, 1989.
- [8] T. Chen and H. Chen. Universal approximation to nonlinear operators by neural networks with arbitrary activation functions and its application to dynamical systems. *IEEE Transactions on Neural Networks*, 6(4):911–917, 1995.
- [9] L. Lu, P. Jin, G. Pang, Z. Zhang, and G.E. Karniadakis. Learning nonlinear operators via DeepONet based on the universal approximation theorem of operators. *Nature Machine Intelligence*, 3(3):218–229, 2021.
- [10] Z. Li, N. Kovachki, K. Azizzadenesheli, B. Liu, K. Bhattacharya, A. Stuart, and A. Anandkumar. Fourier Neural Operator for parametric partial differential equations. *arXiv preprint arXiv:2010.08895*, 2020.
- [11] Z. Li, N. Kovachki, K. Azizzadenesheli, B. Liu, A. Stuart, K. Bhattacharya, and A. Anandkumar. Multipole graph neural operator for parametric partial differential equations. *Advances in Neural Information Processing Systems*, 33:6755–6766, 2020.
- [12] N. Kovachki, Z. Li, B. Liu, K. Azizzadenesheli, K. Bhattacharya, A. Stuart, and A. Anandkumar. Neural operator: Learning maps between function spaces with applications to PDEs. *Journal of Machine Learning Research*, 24(89):1–97, 2023.

- [13] D. Kochkov, J.A. Smith, A. Alieva, Q. Wang, M.P. Brenner, and S. Hoyer. Machine learning-accelerated computational fluid dynamics. *Proceedings of the National Academy of Sciences*, 118(21):e2101784118, 2021.
- [14] W. Xiao, T. Gao, K. Liu, J. Duan, and M. Zhao. Fourier Neural Operator based fluid-structure interaction for predicting the vesicle dynamics. *arXiv preprint arXiv:2401.02311*, 2024.
- [15] S.A. Faroughi, N.M. Pawar, C. Fernandes, M. Raissi, S. Das, N.K. Kalantari, and S. Kourosh Mahjour. Physics-guided, physics-informed, and physics-encoded neural networks and operators in scientific computing: Fluid and solid mechanics. *Journal of Computing and Information Science in Engineering*, 24(4):040802, 2024.
- [16] X. He, L. Yan, L. Jiang, A. Yi, Z. Pu, Y. Yu, H. Chen, W. Pan, and B. Luo. Fourier neural operator for accurate optical fiber modeling with low complexity. *Journal of Lightwave Technology*, 41(8):2301–2311, 2022.
- [17] M. Zhu, H. Zhang, A. Jiao, G.E. Karniadakis, and L. Lu. Reliable extrapolation of deep neural operators informed by physics or sparse observations. *Computer Methods in Applied Mechanics and Engineering*, 412:116064, 2023.
- [18] M. McCabe, P. Harrington, S. Subramanian, and J. Brown. Towards stability of autoregressive neural operators. *arXiv preprint arXiv:2306.10619*, 2023.
- [19] L. Mandl, D. Nayak, T. Ricken, and S. Goswami. Physics-informed time-integrated deepnet: Temporal tangent space operator learning for high-accuracy inference. *arXiv preprint arXiv:2508.05190*, 2025.
- [20] B. Bonev, T. Kurth, C. Hundt, J. Pathak, M. Baust, K. Kashinath, and A. Anandkumar. Spherical fourier neural operators: Learning stable dynamics on the sphere. In *International conference on machine learning*, pages 2806–2823. PMLR, 2023.
- [21] D. Patel, D. Ray, M.R.A. Abdelmalik, T.J.R. Hughes, and A.A. Oberai. Variationally mimetic operator networks. *Computer Methods in Applied Mechanics and Engineering*, 419:116536, 2024.
- [22] K.F. Riley, M.P. Hobson, and S.J. Bence. *Mathematical methods for physics and engineering: a comprehensive guide*. Cambridge University Press, 2006.
- [23] G.E. Karniadakis, I.G. Kevrekidis, L. Lu, P. Perdikaris, S. Wang, and L. Yang. Physics-informed machine learning. *Nature Reviews Physics*, 3(6):422–440, 2021.
- [24] E. Zhang, A. Kahana, A. Kopaničáková, E. Turkel, R. Ranade, J. Pathak, and G.E. Karniadakis. Blending neural operators and relaxation methods in PDE numerical solvers. *Nature Machine Intelligence*, 6(11):1303–1313, 2024.
- [25] J. Hu and P. Jin. A hybrid iterative method based on MIONet for PDEs: Theory and numerical examples. *Mathematics of Computation*, 2025. Published electronically. DOI <https://doi.org/10.1090/mcom/4086>.
- [26] J. Ackmann, P.D. Düben, T.N. Palmer, and P.K. Smolarkiewicz. Machine-learned preconditioners for linear solvers in geophysical fluid flows. *arXiv preprint arXiv:2010.02866*, 2020.
- [27] A. Kopaničáková and G.E. Karniadakis. DeepONet based preconditioning strategies for solving parametric linear systems of equations. *SIAM Journal on Scientific Computing*, 47(1):C151–C181, 2025.
- [28] Y. Xiang. Unsupervised Convolution Neural Operator preconditioning for the solution of some heterogeneous fluid PDEs. *Inria Centre at the University of Bordeaux*, 2025. hal-04886933v2.
- [29] Y. Saad. A flexible inner-outer preconditioned GMRES algorithm. *SIAM Journal on Scientific Computing*, 14(2):461–469, 1993.
- [30] D. Pasetto, M. Ferronato, and M. Putti. A reduced order model-based preconditioner for the efficient solution of transient diffusion equations. *International Journal for Numerical Methods in Engineering*, 109(8):1159–1179, February 2017.

- [31] Y. Bazilevs and T.J.R. Hughes. Weak imposition of Dirichlet boundary conditions in fluid mechanics. *Computers & fluids*, 36(1):12–26, 2005.
- [32] G.H. Golub and C.F. Van Loan. *Matrix computations*. JHU press, 2013.
- [33] J.S.B. van Zwieten, G.J. van Zwieten, and W. Hoitinga. Nutils 8 (software), 2023. Zenodo. DOI <https://doi.org/10.5281/zenodo.10068507>.
- [34] E. Hasani and R.A. Ward. Generating synthetic data for neural operators. *arXiv preprint arXiv:2401.02398*, 2024.
- [35] B. Raonic, R. Molinaro, T. De Ryck, T. Rohner, F. Bartolucci, R. Alaifari, S. Mishra, and E. de Bézenac. Convolutional Neural Operators for robust and accurate learning of PDEs. *Advances in Neural Information Processing Systems*, 36, 2024.

A Derivation of Green's Operators

A.1 Steady Diffusion

To derive the Green's operator for the steady diffusion equation (4.4) as given by (4.2), we follow the approach of Section 2. We start with testing the governing equation against a test function v as

$$-\int_{\Omega} v \nabla \cdot \theta \nabla u d\mathbf{x}' = \int_{\Omega} v f d\mathbf{x}', \quad (\text{A.1})$$

and perform integration by parts twice on the left-hand side of (A.1) to get

$$-\int_{\Omega} u \nabla \cdot \theta \nabla v d\mathbf{x}' + \int_{\Gamma} v \hat{\mathbf{n}} \cdot \theta \nabla u d\mathbf{x}' - \int_{\Gamma} \theta u \hat{\mathbf{n}} \cdot \nabla v d\mathbf{x}' = \int_{\Omega} v f d\mathbf{x}', \quad (\text{A.2})$$

where the first term on the left-hand side is the adjoint term. If we now split the integral in the second and third term over Γ_N and $\Gamma \setminus \Gamma_N$, and over Γ_D and $\Gamma \setminus \Gamma_D$, respectively, and substitute the boundary data η and g , respectively, and rearrange terms such that all unknown terms appear on the left-hand side, we get

$$B[v, u] = L[v], \quad (\text{A.3})$$

where

$$B[v, u] = -\int_{\Omega} u \nabla \cdot \theta \nabla v d\mathbf{x}' - \int_{\Gamma \setminus \Gamma_N} \theta v \hat{\mathbf{n}} \cdot \nabla u d\mathbf{x}' + \int_{\Gamma \setminus \Gamma_D} \theta u \hat{\mathbf{n}} \cdot \nabla v d\mathbf{x}' \quad (\text{A.4})$$

and

$$L[v] = \int_{\Omega} v f d\mathbf{x}' + \int_{\Gamma_N} v \eta d\mathbf{x}' - \int_{\Gamma_D} g \hat{\mathbf{n}} \cdot \nabla v d\mathbf{x}'. \quad (\text{A.5})$$

If we now define the test function v to be a Green's function G that satisfies

$$\begin{cases} -\nabla \cdot \theta(\mathbf{x}') \nabla G(\mathbf{x}, \mathbf{x}') = \delta(\mathbf{x} - \mathbf{x}') & \forall \mathbf{x}' \in \Omega, \\ \theta(\mathbf{x}') G(\mathbf{x}, \mathbf{x}') = 0 & \forall \mathbf{x}' \in \Gamma \setminus \Gamma_N, \\ \hat{\mathbf{n}} \cdot \theta(\mathbf{x}') \nabla G(\mathbf{x}, \mathbf{x}') = 0 & \forall \mathbf{x}' \in \Gamma \setminus \Gamma_D, \end{cases} \quad (\text{A.6})$$

$B[G, u]$ reduces to $u(\mathbf{x})$, and thereby, the weak form A.3 reduces to the Green's operator 4.2.

A.2 Time-Dependent Diffusion

The derivation of the Green's operator for the time-dependent diffusion problem as given by (5.2) is analogous to the Green's function of the steady problem, except that now all functions and basis functions are functions of space and time (\mathbf{x}, t) , and the integrals extend over the space and time domains $\Omega = [0, L]^2$ and $\Delta t_i = [\Delta t, (i+1)\Delta t]$. Additionally, the time derivative in the operator gives rise to a few additional terms in the

weak form. If we test the term of the time derivative $\partial u^{(i)}/\partial t$ against the test function G and integrate by parts, we get

$$\int_{\Omega \times \Delta t_i} v \frac{\partial u^{(i)}}{\partial t} d\mathbf{x}' dt' = \int_{\Omega \times \Delta t_i} \frac{\partial}{\partial t} (v u^{(i)}) d\mathbf{x}' dt' - \int_{\Omega \times \Delta t_i} u^{(i)} \frac{\partial v}{\partial t} d\mathbf{x}' dt'. \quad (\text{A.7})$$

Integrating the first term on the right-hand side gives

$$\int_{\Omega \times \Delta t_i} v \frac{\partial u^{(i)}}{\partial t} d\mathbf{x}' dt' = \int_{\Omega} \left[v u^{(i)} \right]_{t'=i\Delta t}^{t'=(i+1)\Delta t} d\mathbf{x}' - \int_{\Omega \times \Delta t_i} u^{(i)} \frac{\partial v}{\partial t} d\mathbf{x}' dt', \quad (\text{A.8})$$

and substitution of the initial condition $u^{(i)}(i\Delta t) = u^{(i-1)}(i\Delta t)$ gives

$$\begin{aligned} \int_{\Omega \times \Delta t_i} v \frac{\partial u^{(i)}}{\partial t} d\mathbf{x}' dt' &= \int_{\Omega} v((i+1)\Delta t) u^{(i)}((i+1)\Delta t) d\mathbf{x}' - \int_{\Omega} v(i\Delta t) u^{(i-1)}(i\Delta t) d\mathbf{x}' \\ &\quad - \int_{\Omega \times \Delta t_i} u^{(i)} \frac{\partial v}{\partial t} d\mathbf{x}' dt'. \end{aligned} \quad (\text{A.9})$$

Adding all terms of (A.4), which belong to the spatial part $-\nabla \cdot \theta \nabla$ of the operator, we get the weak form

$$B[v, u^{(i)}] = L[v]. \quad (\text{A.10})$$

Here,

$$\begin{aligned} B[v, u^{(i)}] &= \int_{\Omega \times \Delta t_i} u^{(i)} \mathcal{L}^*[\theta] v d\mathbf{x}' dt' - \int_{\Gamma \setminus \Gamma_N \times \Delta t_i} \theta v \hat{\mathbf{n}} \cdot \nabla u^{(i)} d\mathbf{x}' dt' + \int_{\Gamma \setminus \Gamma_D \times \Delta t_i} \theta u^{(i)} \hat{\mathbf{n}} \cdot \nabla v d\mathbf{x}' dt' \\ &\quad + \int_{\Omega} v((i+1)\Delta t) u^{(i)}((i+1)\Delta t) d\mathbf{x}' \end{aligned} \quad (\text{A.11})$$

and

$$L[v] = \int_{\Omega} v(i\Delta t) u^{(i-1)}(i\Delta t) d\mathbf{x}' + \int_{\Omega \times \Delta t_i} v f d\mathbf{x}' dt' + \int_{\Gamma_N \times \Delta t_i} v \eta d\mathbf{x}' dt' - \int_{\Gamma_D \times \Delta t_i} g \hat{\mathbf{n}} \cdot \nabla v d\mathbf{x}' dt', \quad (\text{A.12})$$

where $\mathcal{L}^*[\theta] = -\partial/\partial t - \nabla \cdot \theta \nabla$. If we now define the test function v to be a Green's function G that satisfies

$$\begin{cases} \mathcal{L}^*[\theta] G^{(i)} = \delta & \forall (\mathbf{x}', t') \in \Omega \times \Delta t_i, \\ \theta G^{(i)} = 0 & \forall (\mathbf{x}', t') \in \Gamma \setminus \Gamma_N \times \Delta t_i, \\ \hat{\mathbf{n}} \cdot \theta \nabla G^{(i)} = 0 & \forall (\mathbf{x}', t') \in \Gamma \setminus \Gamma_D \times \Delta t_i, \\ G^{(i)} = 0 & \forall (\mathbf{x}', t') \in \Omega \times \{0\}, \end{cases} \quad (\text{A.13})$$

$B[G, u]$ reduces to $u(\mathbf{x}, t)$, which leaves us with the Green's operator (5.2).

A.3 Advection-diffusion

For the advection-diffusion tests, the NGO formulation is not based directly on Green's function formulation. Instead, we use the weak form derived by Bazilevs and Hughes [31], modified to handle the Neumann/Robin boundary conditions:

$$\begin{aligned} &(-\nabla v, \mathbf{c} u - \theta \nabla u)_\Omega + (\mathbb{L} v \tau, \mathcal{L} u)_\Omega + (v, -\theta \nabla u \cdot \mathbf{n} + \mathbf{c} \cdot \mathbf{n} u)_{\Gamma_D} + (-\gamma \theta \nabla v \cdot \mathbf{n} - \mathbf{c} \cdot \mathbf{n} v, u)_{\Gamma_{D,\text{in}}} \\ &+ (-\gamma \theta \nabla v \cdot \mathbf{n}, u)_{\Gamma_{D,\text{out}}} + \frac{C}{h} (v \theta, u)_{\Gamma_D} + (v, (\mathbf{c} \cdot \mathbf{n})_+ u)_{\Gamma_N} = (v, f)_\Omega + (v, \eta)_{\Gamma_N} + (\mathbb{L} v \tau, f)_\Omega \\ &+ \left(-\gamma \nabla v \cdot \mathbf{n} - \frac{1}{\theta} \mathbf{c} \cdot \mathbf{n} v, g \right)_{\Gamma_{D,\text{in}}} + (-\gamma \nabla v \cdot \mathbf{n}, g)_{\Gamma_{D,\text{out}}} + \frac{C}{h} (v, g)_{\Gamma_D}. \end{aligned}$$

Here, $\mathcal{L} u = -\nabla \cdot (\theta \nabla u) + \mathbf{c} \cdot \nabla u$, $\mathbb{L} v = \mathbf{c} \cdot \nabla v$, and γ is chosen as -1 . In particular, for both data NGOs and model NGOs the right-hand-side vector is computed as

$$L[v] = (v, f)_\Omega + (v, \eta)_{\Gamma_N} + \left(-\gamma \nabla v \cdot \mathbf{n} - \frac{1}{\theta} \mathbf{c} \cdot \mathbf{n} v, g \right)_{\Gamma_{D,\text{in}}} + (-\gamma \nabla v \cdot \mathbf{n}, g)_{\Gamma_{D,\text{out}}}.$$

B Data generation

B.1 Steady Diffusion

To test the efficacy of different model architectures, three different data sets are generated. Note that these are the data sets used to obtain the results presented in Section 4.3.1 and elsewhere, unless otherwise specified.

- For **dataset A**, $N = 10000$ random triples (θ, f, η) are sampled, and the resulting PDE is solved to obtain u . The functions θ are obtained by sampling 10000 independent functions $\hat{\theta}$ from a Gaussian Random Field (GRF) with correlation length $\lambda = 0.4$, after which θ is defined as $\theta_i(\mathbf{x}) = a\hat{\theta}(\mathbf{x}) + b$, where the scalars a, b are chosen such that θ lies in the interval $[0.02, 0.99]$, i.e. $\min_i \min_{\mathbf{x}} \theta_i(\mathbf{x}) = 0.02$ and $\max_i \max_{\mathbf{x}} \theta_i(\mathbf{x}) = 0.99$. The source terms f are generated using the same process, except with $\lambda = 0.2$. Finally η is generated in the same way with $\lambda = 0.3$ and the resulting functions are scaled and shifted to lie in $[-1, 1]$. The Dirichlet boundary data g are identically zero.

To solve the PDEs, we make use of the Nutils [33] finite element solver. The domain is discretized on a 20×20 grid of cubic B-splines (resulting in 23^2 basis functions). Comparing the solutions to those obtained on a 40×40 grid, we find that the numerical solutions have a relative error of about $3 \cdot 10^{-4}$.

- For **dataset B**, solutions are obtained using manufactured solutions [34]. In this approach, the solution u and the parameters θ are randomly generated, after which the source and boundary terms are computed by evaluating the relevant differential operator acting on u . Firstly, the functions θ are generated using the same method as is used in the previous data set, but with smaller characteristic length scale $\lambda = 0.2$. Then, random functions \hat{u} are generated from a GRF with $\lambda = 0.2$, and the solutions are given as $u_i(\mathbf{x}) = x_1(1 - x_1)\hat{u}_i(\mathbf{x})$, so that the solutions satisfy homogeneous Dirichlet boundary conditions. Then, f and η are simply computed by evaluating their corresponding operators in (4.1) through analytical expressions for the relevant derivatives. Finally, for each sample we scale f_i , η_i , and u_i uniformly so that $\|f_i\|_{L^2} = \frac{1}{2}$. This normalization is done to ensure that the inputs η, θ, f are of a similar magnitude to what they are in the training data. For the VarMiON and NGO, the normalization does not affect the model accuracy since these models are linear in f and η . However, DeepONets and FNOs, which do not have this linearity, are expected to perform best when the inputs are of a similar magnitude as the training data.

The first data set will be used for training, validation, and testing, while the second data set will be used only for testing. The reason for this distinction is to test how well models trained on one data set can generalize to differently distributed data. When using models as preconditioners in numerical methods, the expectation is that the model will be used on problems that do not lie in the training data distribution. As such, generalization to such data is considered an important factor for models used as preconditioners.

Dataset C Dataset C consists of 10000 manufactured GRF solutions, defined as

$$u(\mathbf{x}) = b + c \cdot \text{GRF}(\lambda; \mathbf{x}), \quad (\text{B.1})$$

where GRF is a Gaussian random field with correlation length scale λ , scaling c and offset b . We manufacture θ and u by drawing the numbers b, c and λ from the distributions indicated in Table 7 and substituting them in Equation B.1. The corresponding f, η and g were obtained by passing the manufactured θ and u through the respective PDE and boundary operators of 4.1.

Table 7: Distributions used for the Gaussian random field offset b , scaling c and length scale λ/L for the solution u and material parameter θ for dataset C, manufactured using Equation B.1. U is the uniform distribution.

	Offset b	Scaling c	Length scale λ/L
Material parameter θ	1	$U(0, 0.2)$	$U(0.5, 1)$
Solution u	$U(-1, 1)$	$U(0, 1)$	$U(0.5, 1)$

B.2 Time-Dependent Diffusion

Dataset D Dataset D consists of 10000 manufactured GRF solutions, defined as

$$u(\mathbf{x}, t) = b + c \cdot \text{GRF}(\lambda, \tau; \mathbf{x}, t), \quad (\text{B.2})$$

where τ is the timescale of the GRF, that we vary independently of the length scale λ . We manufacture θ and u by drawing the numbers b , c , λ and τ from the distributions indicated in Table 8 and substituting them in Equation B.2. The corresponding u_0 , f , η and g were obtained by passing the manufactured θ and u through the respective PDE and boundary operators of 5.1.

Table 8: Distributions used for the Gaussian random field offset b , scaling c , length scale λ/L and time scale τ/T for the solution u and material parameter θ for dataset C, manufactured using Equation B.2. U is the uniform distribution.

	Offset b	Scaling c	Length scale λ/L	Time scale τ/T
Material parameter θ	1	$U(0, 0.2)$	$U(0.5, 1)$	$U(0.5, 1)$
Solution u	$U(-1, 1)$	$U(0, 1)$	$U(0.5, 1)$	$U(0.5, 1)$

B.3 Advection-Diffusion

Dataset E Solutions to the advection-diffusion equation (5.27) are obtained by drawing random parameters θ , \mathbf{c} , f , g , and η , and subsequently solving for u . The parameters are distributed as follows:

- \mathbf{c} is chosen to be spatially constant, with c_x and c_y both distributed as $\mathcal{N}(\mu = 0, \sigma^2 = 25)$. This produces velocity fields with a uniformly distributed direction. In particular, some sample problems have a velocity field that points towards the left or right boundary, producing a boundary layer there due to the Dirichlet boundary conditions. Other velocity fields point towards the top or bottom boundaries, in which case no boundary layer appears.
- The distribution of θ is chosen as $\theta(\mathbf{x}) = \frac{1}{10} \log \left(e^{0.01} + \exp \left(\hat{\theta}(\mathbf{x}) \right) \right)$ where $\hat{\theta} \sim \text{GRF}(\lambda = 0.4)$. The reason for this distribution is to ensure positivity of θ (in this case $\theta > 0.001$), while also allowing the ratio $\frac{\max_{\mathbf{x}} \theta(\mathbf{x})}{\min_{\mathbf{x}} \theta(\mathbf{x})}$ to be high, i.e. ensuring that θ is not approximately constant.
- The other fields are chosen as $f \sim \text{GRF}(\lambda = 0.4)$, $g \sim 0.005 \text{GRF}(\lambda = 0.4)$ and $\eta \sim 0.5 \text{GRF}(\lambda = 0.4)$. For the boundary data g and η , the left and right (resp. top and bottom) segments are generated independently. The scaling factors for g and η are chosen such that all three terms of f, g, η contribute significantly to the solution.

Given these parameters, the PDEs are solved on a 53×53 cubic B-spline basis (i.e. with a mesh size of $h = \frac{1}{50}$), using the stabilized weak form of Bazilevs and Hughes [31].

C Model architectures

C.1 Steady Diffusion

C.1.1 Architectures of Section 4.3.1

Figure 22 shows the architectures of the DeepONet, FNO, and VarMiON. Figure 23 shows the architectures of the NGOs. The architectures of the system networks for the VarMiON and NGOs are shown in Figure 24. The U-Net architectures for the data NGO and VarMiON are identical with exception of the number of channels in the hidden layers. This is due to the extra 144×144 linear layer in the VarMiON, which means that the U-Net must have fewer parameters in order to keep the total parameter count approximately the same.

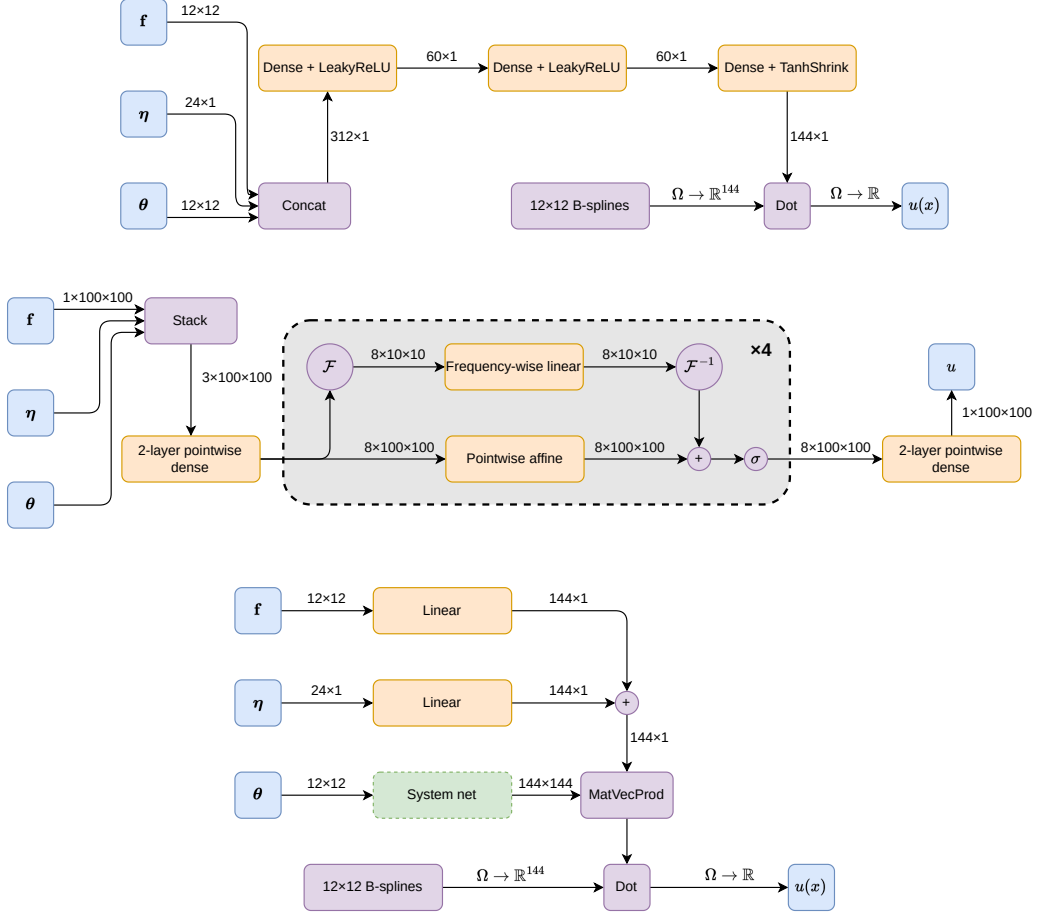


Figure 22: From top to bottom: architectures of the DeepONet, FNO, and VarMiON.

C.1.2 Architectures of Section 4.3.2

The architectures of the different models used in Section 4.3.2 follow the structure of those presented in Section C.1.1, except that the learnable component in the DeepONet is a U-Net instead of an MLP, and that the models accept the Dirichlet boundary condition g as an additional input function. Furthermore, the models use bases and quadrature grids of slightly different sizes, and therefore, the used NN architectures have different input and output shapes. The structure of the input and output shapes of the learnable components are clarified in Table 9, together with the used mathematical model definitions. Table 10 contains the specific settings used regarding the basis, quadrature and learnable model component. For reproducibility, the specific system net settings used are included in Table 11. The number of channels of the NN architectures have been used to equalize their trainable parameter counts to approximately 30000.

C.1.3 System net architectures of Section 4.3.3

The four system nets used in Figure 10 are defined as follows:

- **MLP (multilayer perceptron):** a 4 layer multilayer perceptron with ReLU activations and zero biases. The input and output shapes have been properly adjusted to match the data, and the (equal) width of the hidden layers has been used to adjust the number of trainable parameters to approximately $3 \cdot 10^4$.
- **CNN (convolutional neural network):** the CNN follows the structure of the bottom model of Figure 24, without skip connections. The kernel, input and output shapes are mentioned in Tables 9, 10 and 11.

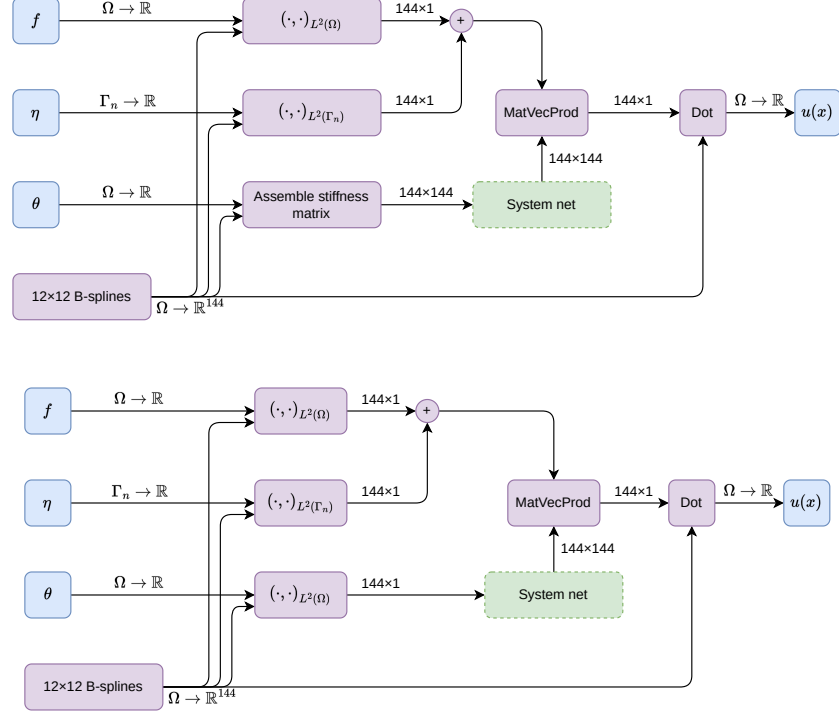


Figure 23: Architecture of the model NGO (top) and data NGO (bottom).

Table 9: The mathematical definitions of the models used to produce the results in Section 4.3.2, together with the input and output shapes of the learnable components (or system nets) of these models. Hats indicate quantities learned by NNs. $\hat{\theta} := \{\hat{\theta}_i\}_{i=1}^{n_\theta}$ and $\hat{f} := \{\hat{f}_i\}_{i=1}^{n_f}$ denote the set of all n_θ PDE coefficient fields and n_f inhomogeneity fields (forcings and boundary conditions), respectively. Q_x and Q_y denote the number of quadrature points \mathbf{x}_q in directions x and y , respectively. N_x and N_y denote the number of basis functions ϕ_m in directions x and y , respectively, and $N = N_x N_y$ is the total number of basis degrees of freedom. $\mathbf{F}[\theta]$ is defined by Equation 4.7 for the data NGO and by Equation 4.6 for the data-free and model NGO, respectively. The right-hand side vector d_n is defined by Equation 4.4. A VarMiON learns \hat{d}_n using a single layer MLP $\hat{F}_{i,nq}$ for every discretized inhomogeneity field $f_i(\mathbf{x}_{i,q})$.

	Definition	NN input shape	NN output shape
NN (U-Net)	$\hat{u}(\mathbf{x}_q) = \hat{u}(\hat{\theta}(\mathbf{x}_q), \hat{f}(\mathbf{x}_q))$	$(n_\theta + n_f, Q_x, Q_y)$	(Q_x, Q_y)
DeepONet	$\hat{u}(\mathbf{x}) = \hat{u}_m(\hat{\theta}(\mathbf{x}_q), \hat{f}(\mathbf{x}_q)) \phi_m(\mathbf{x})$	$(n_\theta + n_f, Q_x, Q_y)$	(N_x, N_y)
VarMiON	$\hat{u}(\mathbf{x}) = \hat{A}_{mn}(\hat{\theta}(\mathbf{x}_q)) \hat{d}_n(\hat{f}(\mathbf{x}_q)) \phi_m(\mathbf{x})$ where $\hat{d}_n(\hat{f}(\mathbf{x}_q)) = \sum_i \hat{F}_{i,nq} f_i(\mathbf{x}_{i,q})$	(n_θ, Q_x, Q_y)	(N, N)
Data NGO	$\hat{u}(\mathbf{x}) = \hat{A}_{mn}(\mathbf{F}[\theta]) d_n[\hat{f}] \phi_m(\mathbf{x})$	(n_θ, N_x, N_y)	(N, N)
Data-free NGO	$\hat{u}(\mathbf{x}) = \hat{A}_{mn}(\mathbf{F}[\theta]) d_n[\hat{f}] \phi_m(\mathbf{x})$	(N, N)	(N, N)
Model NGO	$\hat{u}(\mathbf{x}) = \hat{A}_{mn}(\mathbf{F}[\theta]) d_n[\hat{f}] \phi_m(\mathbf{x})$	(N, N)	(N, N)
FNO	$\hat{u}(\mathbf{x}_q) = \hat{u}(\hat{\theta}(\mathbf{x}_q), \hat{f}(\mathbf{x}_q))$	$(n_\theta + n_f, Q_x, Q_y)$	(Q_x, Q_y)

- U-Net: the U-Net follows the structure of the bottom model of Figure 24. The kernel, input and output shapes are mentioned in Tables 9, 10 and 11.
- FNO (fourier neural operator): the FNO follows the structure shown in Figure 22. The kernel, input and output shapes are mentioned in Tables 9, 10 and 11.

Table 10: Specific settings used for the different models of Section 4.3.2 regarding basis, quadrature and system net. N_x , N_y , Q_x and Q_y are the number of basis functions and quadrature points, respectively, in directions x and y , respectively. The U-Nets and FNO follow the structure of Figures 22 and 24.

	Basis		Quadrature		System Net	
	Type	(N_x, N_y)	Type	(Q_x, Q_y)	Type	#params
NN (U-Net)	-	-	Uniform	(100, 100)	U-Net	28770
DeepONet	B-splines	(10, 10)	Uniform	(100, 100)	U-Net	28878
VarMiON	B-splines	(10, 10)	Uniform	(10, 10)	U-Net	29072
Data NGO	B-splines	(10, 10)	Gaussian	(99, 99)	U-Net	29482
Data-free NGO	B-splines	(10, 10)	Gaussian	(99, 99)	U-Net	28590
Model NGO	B-splines	(10, 10)	Gaussian	(99, 99)	U-Net	28590
FNO	Fourier modes	(10, 10)	Uniform	(100, 100)	FNO	29128

Table 11: Specific settings of the system nets used by the different models of Section 4.3.2.

	Channels	Kernel sizes (= strides)
NN (U-Net)	15	(2,2), (2,2), (5,5), (5,5), (5,5), (5,5), (2,2), (2,2)
DeepONet	18	(10,10), (1,1), (2,2), (5,5), (5,5), (2,2), (1,1), (1,1)
VarMiON	12	(1,1), (1,1), (2,2), (5,5), (5,5), (2,2), (1,1), (10,10)
Data NGO	22	(1,1), (1,1), (2,2), (5,5), (5,5), (2,2), (1,1), (10,10)
Data-free NGO	15	(2,2), (2,2), (5,5), (5,5), (5,5), (5,5), (2,2), (2,2)
Model NGO	15	(2,2), (2,2), (5,5), (5,5), (5,5), (5,5), (2,2), (2,2)
FNO	7	-

C.2 Time-Dependent Diffusion

The model architectures of Section 5.1 follow the definitions presented in Table 9, except that the bases ϕ_m now depend on space-time (\mathbf{x}, t) and that the quadrature is now defined on the space-time domain shown in Figure 13. The settings of the different neural operators regarding the basis, system net, quadrature and number of trainable parameters are presented in Table 12. For reproducibility, the specific system net settings used are included in Table 13.

Table 12: Specific settings used for the different models of Section 5.1 regarding basis, quadrature and system net. N_t , N_x , N_y , Q_t , Q_x and Q_y are the number of basis functions and quadrature points, respectively, in directions t , x and y , respectively. The U-Nets and FNO follow the structure of Figures 22 and 24.

	Basis		Quadrature		System Net	
	Type	(N_t, N_x, N_y)	Type	(Q_t, Q_x, Q_y)	Type	#params
NN (U-Net)	-	-	Uniform	(2, 100, 100)	U-Net	29702
DeepONet	B-splines	(2, 10, 10)	Uniform	(2, 100, 100)	U-Net	29141
VarMiON	B-splines	(2, 10, 10)	Uniform	(2, 5, 5)	U-Net	29638
Data NGO	B-splines	(2, 10, 10)	Gaussian	(2, 99, 99)	U-Net	29008
Data-free NGO	B-splines	(2, 10, 10)	Gaussian	(2, 99, 99)	U-Net	26556
Model NGO	B-splines	(2, 10, 10)	Gaussian	(2, 99, 99)	U-Net	26556
FNO	Fourier modes	(2, 10, 10)	Uniform	(2, 100, 100)	FNO	28734

For the time-dependent diffusion problem, the architecture of the data NGO is slightly different than for the steady diffusion problem: for the time-dependent diffusion problem, we provide the data NGOs the additional fixed input $F_{t,n} \equiv \int_{\Omega} \psi_n ((i+1)\Delta t) d\mathbf{x}'$. The reason why we do this is that otherwise the system net that we use, a U-Net with ReLU activations and zero bias, exhibits an unwanted symmetry that is not present in the training data. A ReLU activation function exhibits the scale equivariance property

$$\text{ReLU}(c\mathbf{x}) = c\text{ReLU}(\mathbf{x}) \quad \forall c \in \mathbb{R}^+, \quad (\text{C.1})$$

Table 13: Specific settings of the system nets used by the different models of Section 5.1.

	Channels	Kernel sizes (= strides)
NN (U-Net)	11	(1,2,2), (1,2,2), (1,5,5), (2,5,5), (2,5,5), (1,5,5), (1,2,2), (1,2,2)
DeepONet	11	(1,10,10), (1,1,1), (1,2,2), (2,5,5), (2,5,5), (1,2,2), (1,1,1), (1,1,1)
VarMiON	2	(1,1,1), (1,1,1), (1,1,1), (2,5,5), (5,5), (1,1), (1,1), (40,40)
Data NGO	14	(1,1,1), (1,1,1), (1,2,2), (2,5,5), (5,5), (2,2), (1,1), (20,20)
Data-free NGO	6	(2,2), (2,2), (5,5), (10,10), (10,10), (5,5), (2,2), (2,2)
Model NGO	6	(2,2), (2,2), (5,5), (10,10), (10,10), (5,5), (2,2), (2,2)
FNO	7	-

and since a U-Net with ReLU activations and zero bias consists only of linear maps and ReLU activations, the U-Net as a whole exhibits the same scale equivariance property

$$\text{NN}(c\mathbf{x}) = c\text{NN}(\mathbf{x}) \quad \forall c \in \mathbb{R}^+. \quad (\text{C.2})$$

The mapping that the system net intends to learn is not scale equivariant in this sense, so we do not want the system net to have this property either. Adding a constant input to $F_{t,n} \equiv \int_{\Omega} \psi_n((i+1)\Delta t) d\mathbf{x}'$ breaks this unwanted symmetry. \mathbf{F}_t enters the U-Net via a separate input channel. Adding \mathbf{F}_t as input did not significantly change the accuracy of the data NGO on the tests performed in Section 5.1, however, it did result in slightly faster convergence of the training.

C.3 Advection Diffusion

The architectures of the NGOs are largely unchanged from their architectures in Section 4.3.1. The differences are listed here:

- Model NGOs construct the input matrix using the weak form from Bazilevs and Hughes [31], modified to handle the different boundary conditions (the cited paper assumes Dirichlet boundary conditions on the entire boundary). However, model NGOs omit the SUPG term and Dirichlet penalty term (the third and last terms of equation (10) of Bazilevs and Hughes). These were found not to have a positive effect on the model accuracy, and as such they are omitted to improve the computational efficiency of the model.
- Data NGOs construct the input matrix by integrating θ , c_x , and c_y against the B-spline basis. The output matrix is multiplied by the same right-hand-side vector as is used in model NGOs. In particular, this means that the right-hand-side vector is also assembled using the unstabilized part of the weak form of Bazilevs and Hughes [31].
- For DeepONets and VarMiONs, the inputs are θ, c_x, c_y, f, g , and η . The fields θ, c_x, c_y , and f are sampled on a 12×12 uniform grid, whereas the boundary data g and η are sampled on 2×12 points each, namely on 12 points per boundary segment. Note that this means that DeepONets and VarMiONs are given much coarser information about the inputs than other models. As explained, however, the architectures of these models do not allow for the inputs to be sampled more finely without drastically increasing the model's parameter count.
- For FNOs, CNOs, and U-Nets, the inputs are θ, c_x, c_y, f, g , and η , all sampled on a 100×100 uniform grid. Since η and g are only defined on the boundaries, their values are extended to the entire domain via nearest-neighbor resampling.

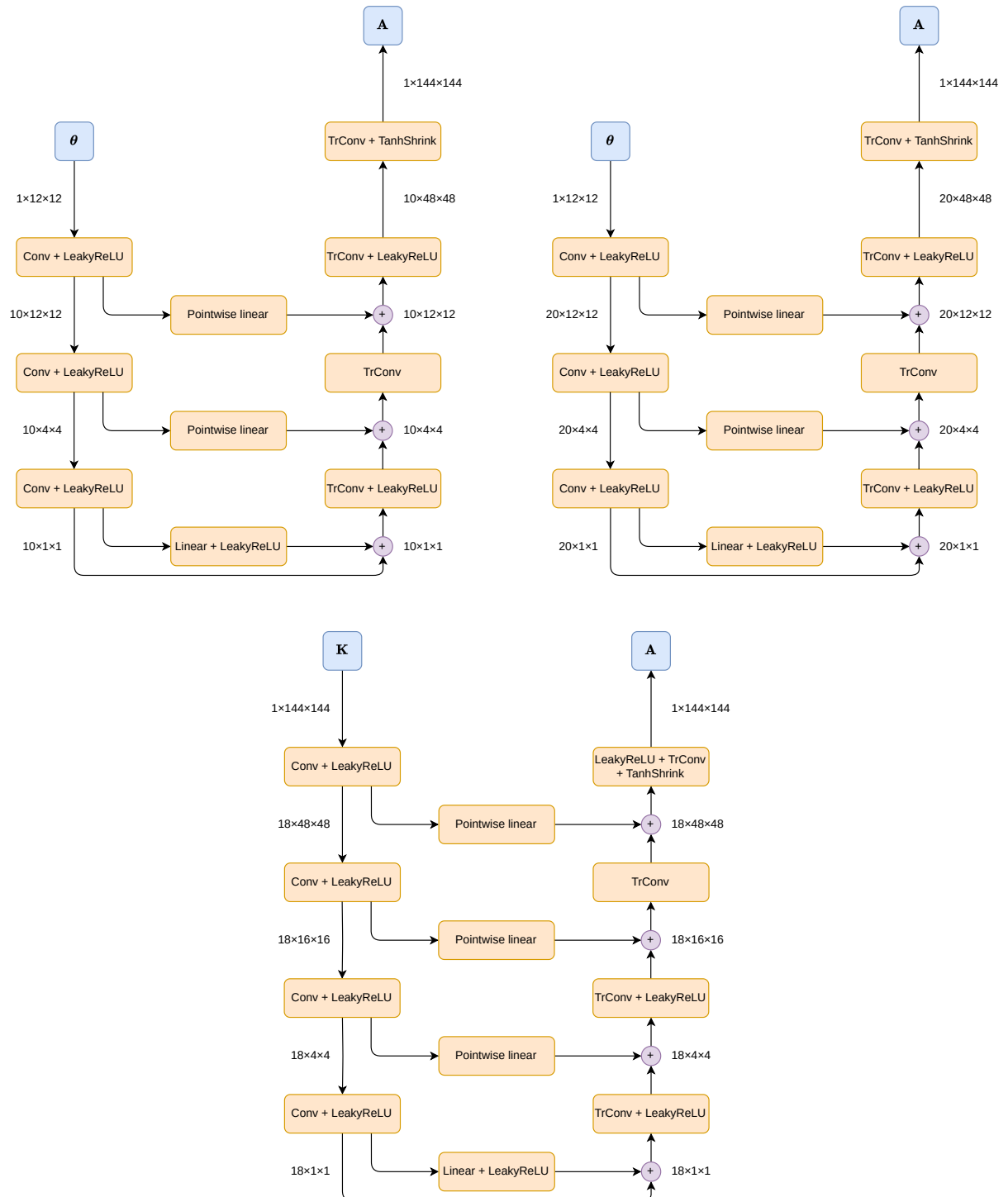


Figure 24: U-Net (system) architectures of the VarMiON (top left), data NGO (top right), and model NGO (bottom).

D Training Procedure

D.1 Steady Diffusion

D.1.1 Training procedure for Tests in Sections 4.3.1, 4.3.5 and 4.3.6

The training procedure is the same for each model. The model is trained on the first 8000 samples of the first dataset. After every epoch, the model is evaluated on the validation data (another 1000 samples from the first data). The final trained model is the model that performs best on the validation data. Table 14 shows the training configuration.

Table 14: Configuration of the training procedure

Loss function	Relative L^2 error
Optimizer	ADAM
Learning rate	Default (10^{-3})
Batch size	100
Training time	20000 epochs
Training data	Samples 1 – 8000
Validation data	Samples 8001 – 9000
Testing data (in distribution)	Samples 9001 – 10000
Testing data (out of distribution)	All 1000 manufactured samples

D.1.2 Training procedure for Tests in Sections 4.3.2, 4.3.3 and 4.3.4

The training settings of the models corresponding to the results of Sections 4.3.2, 4.3.3 and 4.3.4 are identical to those presented in Table 14, except that 10000 samples have been used for training and 1000 samples for validation, and that the data-free NGO and model NGO have been trained for 5000 epochs only.

D.2 Time-Dependent Diffusion

The training settings used for the time-dependent diffusion problem are identical to those of the steady diffusion problem as presented in Table 14, except that 10000 samples have been used for training and 1000 samples for validation, and that the data-free NGO and model NGO have been trained for 5000 epochs only. The inductive bias for time stepping stability as presented in Section 5.1.2 is all included in the forward and backward passes of the training loop. To estimate the norm of the update matrix $\|\hat{\mathbf{A}}^{(i)}\mathbf{M}_{lr}\|_{\mathbf{M}_{rr}}$ in the norm scaling layer in the data NGO, we use a power iteration [32]

$$\lambda, \mathbf{v} \approx \text{PowerIteration}(\mathbf{B}; \lambda_0, \mathbf{v}_0), \quad (\text{D.1})$$

where \mathbf{B} is a square matrix, λ_0 and \mathbf{v}_0 are initial guesses for the dominant eigenvalue and eigenvector of \mathbf{B} , respectively, and λ and \mathbf{v} are power iteration approximations of the dominant eigenvalue and eigenvector of \mathbf{B} , respectively. The initial guess for the dominant eigenvalue λ_0 is set to 1, and kept fixed. To speed up the convergence of the power iterations, we update the initial guess \mathbf{v}_0 during training after every epoch as

$$\lambda_0, \mathbf{v}_0 \leftarrow \text{PowerIteration}\left(\hat{\mathbf{A}}[\langle\theta\rangle]\mathbf{M}_{lr}; \lambda_0, \mathbf{v}_0\right). \quad (\text{D.2})$$

In words, we "learn" during training the dominant eigenvector corresponding to the matrix $\hat{\mathbf{A}}[\langle\theta\rangle]\mathbf{M}_{lr}$, and use this as initial guess \mathbf{v}_0 for other matrices $\hat{\mathbf{A}}^{(i)}\mathbf{M}_{lr}$. Since all material parameters θ are centered and reasonably close to $\langle\theta\rangle = 1$, the dominant eigenvector \mathbf{v}_0 of the matrix $\hat{\mathbf{A}}[\langle\theta\rangle]\mathbf{M}_{lr}$ is a good initial guess for the dominant eigenvector \mathbf{v} of the matrices $\hat{\mathbf{A}}^{(i)}\mathbf{M}_{lr}$. A power iteration then typically takes 2-10 iterations to converge.

D.3 Advection-Diffusion

The training procedure for advection-diffusion is the same as that for steady diffusion (Appendix D.1).

E Scale Equivariance

In this section, we show how to embed into the NGO formulation the scale equivariance of a PDE with respect to its material parameter, in the sense of Equation 4.15. If a PDE is scale equivariant in the sense of Equation 4.15, the Green's function exhibits a similar property. By substituting $\theta' = c\theta$ into (2.6), we get

$$\mathcal{L}^*[\theta']G[\theta'] = \mathcal{L}^*[c\theta]G[c\theta] = c\mathcal{L}^*[\theta]G[c\theta] = \delta, \quad \forall c \in \mathbb{R}^+. \quad (\text{E.1})$$

Combining Equations (E.1) and (2.6) gives

$$G[c\theta] = \frac{1}{c}G[\theta], \quad \forall c \in \mathbb{R}^+. \quad (\text{E.2})$$

Equation (2.8) tells us that we can embed this scale equivariance property into the neural Green's function \hat{G} by making sure that

$$\hat{A}_{mn}[c\theta] = \frac{1}{c}\hat{A}_{mn}[\theta], \quad \forall c \in \mathbb{R}^+. \quad (\text{E.3})$$

If we redefine our neural network \hat{A}_{mn} as

$$\hat{A}'_{mn}(\mathbf{F}[\theta]) \equiv \frac{1}{\|\theta\|}\hat{A}_{mn}\left(\frac{\mathbf{F}[\theta]}{\|\theta\|}\right), \quad (\text{E.4})$$

where $\|\cdot\|$ is a scale equivariant norm, \hat{A}'_{mn} satisfies the scale equivariance property (E.3), since

$$\begin{aligned} \hat{A}'_{mn}(\mathbf{F}[c\theta]) &= \frac{1}{\|c\theta\|}\hat{A}_{mn}\left(\frac{\mathbf{F}[c\theta]}{\|c\theta\|}\right) = \frac{1}{c\|\theta\|}\hat{A}_{mn}\left(\frac{c\mathbf{F}[\theta]}{c\|\theta\|}\right) = \frac{1}{c}\frac{1}{\|\theta\|}\hat{A}_{mn}\left(\frac{\mathbf{F}[\theta]}{\|\theta\|}\right) \\ &= \frac{1}{c}\hat{A}'_{mn}(\mathbf{F}[\theta]). \end{aligned} \quad (\text{E.5})$$

In Figure 25, we show the effect if embedding scale equivariance into a preconditioned model NGO. Details

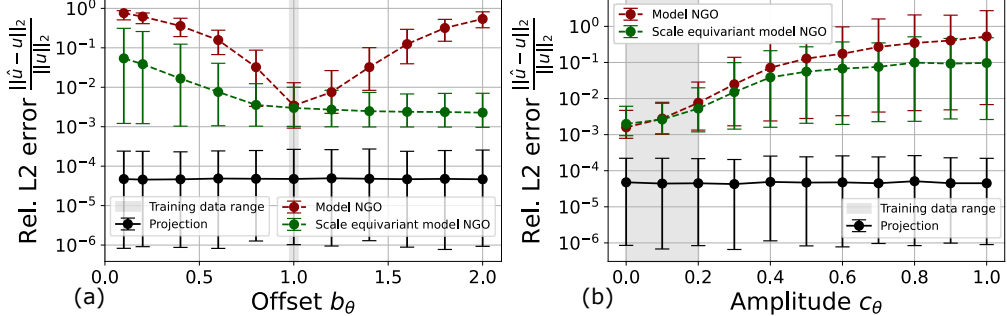


Figure 25: Relative test L^2 error of model NGOs with and without embedded scale equivariance, versus the (a) offset b_θ and (b) amplitude c_θ of the material parameter $\theta(\mathbf{x}) = b_\theta + c_\theta \text{GRF}_{\lambda_\theta}(\mathbf{x})$. The model architectures are presented in C.1.2, and the models have been trained on dataset C (Appendix B). The scale equivariance makes the NGO more robust against scale variations in the material parameter $\theta(\mathbf{x})$. Points and error bars are, respectively, averages and 95% confidence intervals on 1000 manufactured steady diffusion solutions, generated in the same way as dataset C (Appendix B).

of the model architectures are highlighted in Appendix C.1.2. The models have been trained on dataset C, described in Appendix B.1, using the training procedure described in Appendix D.1.2. It can be observed in Figure 25 that embedding scale equivariance into an NGO results in more robustness in scale variations in a material parameter θ manufactured according to (B.1). The reason why the error still increases for small b_θ is that the output of a scale equivariant system net as given by (E.4) is divided by an increasingly small number $\|\theta\|$, which amplifies the prediction error of \hat{A}_{mn} .

F Kronecker Product Assembly of the System Matrix

We first project the material parameters onto the basis given by (5.7) as

$$\theta(\mathbf{x}, t) \approx \boldsymbol{\theta}^T \boldsymbol{\psi}(\mathbf{x}, t) = \boldsymbol{\theta}^T (\boldsymbol{\psi}^{(t)}(t) \otimes_K \boldsymbol{\psi}^{(x)}(x) \otimes_K \boldsymbol{\psi}^{(y)}(y)), \quad (\text{F.1})$$

where $\boldsymbol{\theta} \equiv \{\hat{\theta}_l\}_{l=1}^N$. This enables us to factorize the 3D integrals in the system matrix into three 1D integrals as

$$\begin{aligned} F_{ik}[\theta] &\sim \int_{\Omega \times \Delta t_i} \phi_i \mathcal{L}^*[\theta] \psi_k d\mathbf{x}' dt' \approx \sum_{j=1}^N \hat{\theta}_j \int_{\Omega \times \Delta t_i} \phi_i \mathcal{L}^*[\psi_j] \psi_k d\mathbf{x}' dt' \\ &= \sum_{j=1}^N \hat{\theta}_j (\mathbf{F}^{(t)} \otimes_K \mathbf{F}^{(x)} \otimes_K \mathbf{F}^{(y)})_{ijk} \quad \forall i, k \in \{1, 2, \dots, N\}, \end{aligned} \quad (\text{F.2})$$

where

$$\begin{aligned} \mathbf{F}^{(t)} &= \int_0^T \phi^{(t)} \otimes \mathcal{L}^*[\boldsymbol{\psi}^{(t)}] \otimes \boldsymbol{\psi}^{(t)} dt', \\ \mathbf{F}^{(x)} &= \int_0^L \phi^{(x)} \otimes \mathcal{L}^*[\boldsymbol{\psi}^{(x)}] \otimes \boldsymbol{\psi}^{(x)} dx', \\ \mathbf{F}^{(y)} &= \int_0^L \phi^{(y)} \otimes \mathcal{L}^*[\boldsymbol{\psi}^{(y)}] \otimes \boldsymbol{\psi}^{(y)} dy', \end{aligned} \quad (\text{F.3})$$

and where \otimes is the outer product. We compute $\mathbf{F}^{(t)}$, $\mathbf{F}^{(x)}$ and $\mathbf{F}^{(y)}$ once offline, and save them in memory, and assemble $F_{ik}[\theta]$ using (F.2).

G Relation to CNOs

A Neural Operator architecture similar to NGOs is the Convolutional Neural Operator (CNO) [35]. In a CNO, the input function(s), defined on a rectangular domain in \mathbb{R}^d , are passed through a low-pass filter, creating band-limited functions that can be reconstructed exactly from their samples on a relatively coarse grid. The band-limited function is then sampled on this grid, providing the inputs to a U-Net. The U-Net outputs are then treated as samples of band-limited functions from which the output functions are interpolated. The interpolation also assumes that the samples are of band-limited functions, so that there is a unique band-limited interpolated function.

Both the filtering and sampling of the inputs and the interpolation of the outputs are done through FFTs. In particular, both processes are linear meaning that applying them to standard basis vectors reveals an effective function basis that CNOs operate on. In 1D, the output interpolation can be seen as an expansion in terms of a function basis, where the basis functions are the Dirichlet Kernels $D_n(x - x_k) = 1 + 2 \sum_{i=1}^{\lfloor n/2 \rfloor} \cos(2\pi i(x - x_k)) = \frac{\sin(n\pi(x - x_k))}{\sin(\pi(x - x_k))}$ with $x_k = \frac{k}{n}L$. In 2D, the basis functions are the tensor products $\phi_{kl}(x, y) = D_{n_1}(x - x_k)D_{n_2}(y - y_l)$. The input filtering, being up to a multiplicative constant the adjoint of the output interpolation, is equivalent to integration of the input functions against these basis functions with a uniform quadrature rule.

Figures 26 and 27 show the encoding and decoding process as done in CNOs. Figure 28 shows the function basis corresponding to these encoding and decoding processes. This shows that CNOs use a specific function basis, which can actually be changed based on the problem. For example, while CNOs assume periodic domains, their Dirichlet kernel basis can be replaced by another basis, such as a B-spline basis, that conforms to the topology of the domain.

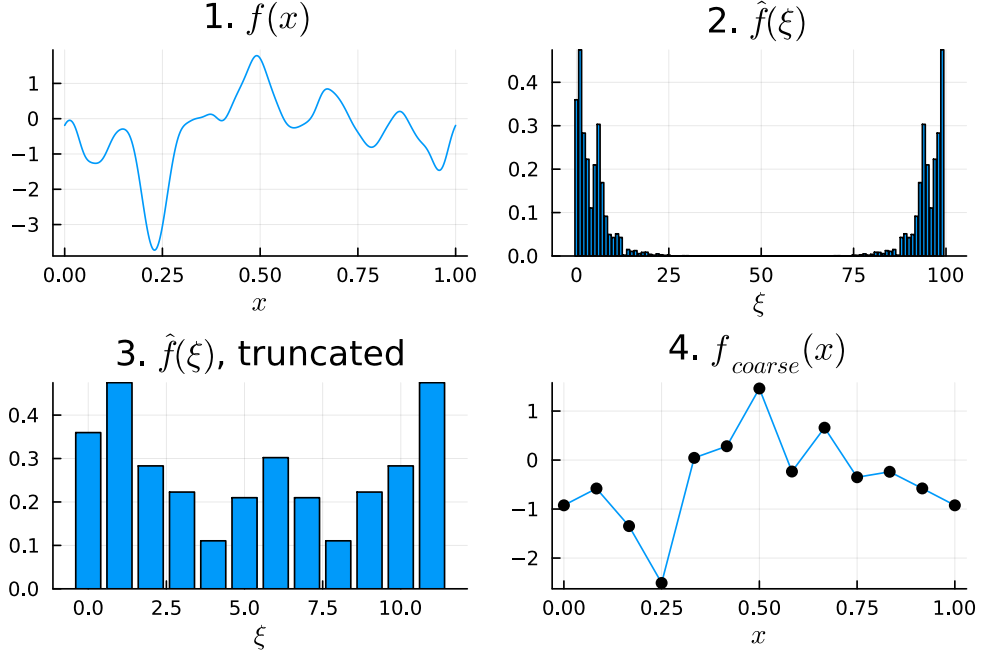


Figure 26: An overview of the filtering process as done in CNOs. A function f on a fine grid (1) is Fourier transformed (2). Then, only the lowest Fourier modes are retained (3). Finally, performing an inverse FFT produces the filtered function on a coarse grid (4).

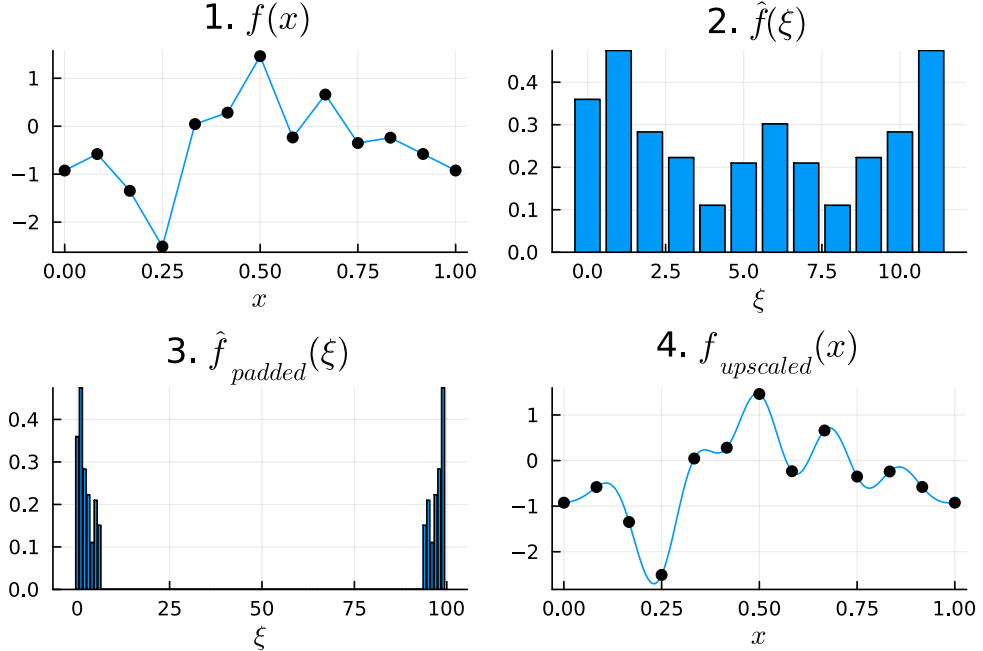


Figure 27: An overview of the interpolation process as done in CNOs. A function on a coarse grid (1) is Fourier transformed (2). Then, zeros are inserted for the high-frequency coefficients (3). Finally, performing an inverse FFT produces an interpolant on a fine grid (4).

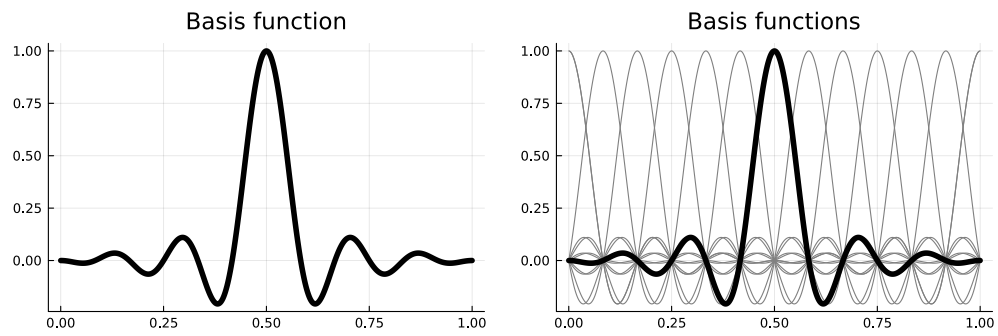


Figure 28: Left: a single Dirichlet kernel basis function. Right: a full function basis, showing that these basis functions are nodal and form a partition of unity.